Large-scale physical modelling of static liquefaction in gentle submarine slopes

Maghsoudloo, Arash; Askarinejad, Amin; de Jager, Richard R.; Molenkamp, Frans; Hicks, Michael A.

DOI
10.1007/s10346-021-01705-6

Publication date
2021

Document Version
Final published version

Published in
Landslides

Citation (APA)
Maghsoudloo, A., Askarinejad, A., de Jager, R. R., Molenkamp, F., & Hicks, M. A. (2021). Large-scale physical modelling of static liquefaction in gentle submarine slopes. *Landslides*, *18*(10), 3315-3335. https://doi.org/10.1007/s10346-021-01705-6

Landslides (2021) 18:3315–3335
DOI 10.1007/s10346-021-01705-6
Received: 30 December 2019
Accepted: 26 May 2021
Published online: 29 June 2021

Arash Maghsoudloo · Amin Askarinejad · Richard R. de Jager · Frans Molenkamp · Michael A. Hicks

Large-scale physical modelling of static liquefaction in gentle submarine slopes

Abstract Planning a monitoring campaign for a natural submarine slope prone to static liquefaction is a challenging task due to the sudden nature of flow slides. Therefore, gaining a better insight by monitoring the changes in pore pressure and acceleration of the soil mass, prior to and at the onset of static liquefaction, of submerged model slopes in the laboratory, helps in quantifying the minimum required triggering levels and ultimately the development of effective margins of safety for this specific failure mechanism. This study presents a set of physical model tests of submarine flow slides in the large-scale GeoTank (GT) of Delft University of Technology, in which a tilting mechanism was employed to trigger static liquefaction in loosely packed sand layers. Novel sensors were developed to locally monitor the hydro-mechanical soil responses acting as precursors of the onset of instability. The measurements indicated that soil instability can initiate at overly gentle slope angles (6–10°) and generate significant excess pore water pressures that intensify the deformations to form a flow slide. Moreover, it was observed that the onset of instability and its propagation are highly dependent on the rate of shear stress change and the state of the soil. The obtained data can be used for the future validation of numerical models for submarine flow slides.

Keywords Loose sands · Onset of instability · Physical modelling · Static liquefaction · Submarine flow slides

Introduction

Flow slides have been classified as one of the types of submarine mass movement (Locat 2001), and they are amongst the most common types of failure of submerged slopes in deltaic areas (Koppejan et al. 1948; Kramer 1988; Lade and Yamamuro 2012; De Groot et al. 2019). This paper is part of a wider research project, investigating liquefaction-induced flow slides in the slopes of scour holes formed in the vicinity of the Eastern Scheldt storm surge barrier in the province of Zeeland in the Netherlands. Several such flow slides have been observed in this area (Silvis and De Groot 1995; Van Velzen et al. 2014; Mastbergen et al. 2016). The stability of the slopes has here been investigated from a geotechnical engineering perspective, whereas the scouring processes and associated hydraulic boundary conditions will be elaborated elsewhere.

Several researchers have listed contributing factors in the triggering of submarine flow slides (Kramer 1988; Hicks and Boughrarou 1998; Sassa and Sekiguchi 2001; Miyamoto et al. 2004; Hicks and Onisiphorou 2005; Masson et al. 2006; Lade and Yamamuro 2011; Sumer 2014). These include wave actions, scouring, water currents, sea level changes, soil variability, seismic loads, and construction loads (e.g. loading during the construction of hydraulic fills and unloading and imposed pressure variations during dredging). Indeed, submarine slope failures are generally initiated by a combination of several causes and the initiation (hydro-mechanical instability) and progression of the failure are highly dependent on the soil response in the presence of the triggers. Liquefaction under static (and pseudo-static) conditions, so-called static liquefaction, has been defined as a consequence of pre-failure soil instability (Lade et al. 1988; Molenkamp 1991; Lade 1992; Terzaghi et al. 1996; Chu and Leong 2001). At the onset of soil instability, a sudden collapse of the metastable soil structure results in a rapid generation of excess pore pressure and a significant loss of effective stresses, and thereby to liquefaction (Sladen et al. 1985; Lade et al. 1988; Stoutjesdijk et al. 1998; Lade and Yamamuro 2011). In addition to the presence of a triggering mechanism, liquefaction-induced flow slides may also occur when submerged slopes formed in liquefiable soils have an unfavourable geometry (Stoutjesdijk et al. 1995). The nature of submarine slides by the static liquefaction of bulk volumes of very loose sand often leads to catastrophic dynamic failures which depend on the slope geometry and triggering intensity. The resulting flow slides involve potentially large liquefied bulk volumes flowing over large distances and potentially induce tsunami-like phenomena. Such failures may be contrasted with the progressive nature of failures in denser sands, which often involve stable propagating retrogressive shear bands in combination with simultaneous pore water seepage for redistributing excess pore pressures (Puzrin et al. 2015; Zhang et al. 2017).

Unfortunately, there are relatively few well-documented liquefaction-induced flow slide case histories, due to their sudden initiation and unpredictability (De Jager 2018). However, uniform loose sands and silty sands have been reported as the dominant soil type in published soil investigations of flow slide case histories worldwide (Koppejan et al. 1948; Olson et al. 2000; Lade and Yamamuro 2012). The subsoil in the estuaries of the Netherlands consist of alternating layers of loosely packed sand that are susceptible to liquefaction and sand in a more densely packed state (De Groot et al. 2012; Mastbergen et al. 2016).

In recent decades, many researchers have tried to characterise the soils that are prone to liquefaction using conventional in situ (e.g. cone penetration test (CPT)) and laboratory (e.g. triaxial) tests (Casagrande 1936; Lindenberg and Koning 1981; Chu and Leong 2001; Chu et al. 2003; Robertson 2009; Sadrekarimi 2014; Dong et al. 2015; Jefferies and Been 2015). The critical density of sands (Lindenberg and Koning 1981), in situ relative density and soil behavioural charts obtained from CPT test results (Robertson 1999; Robertson 2009), coefficient of volume compressibility (Monkul et al. 2014), and state parameter (Been and Jefferies 1985) that measures the distance between the current void ratio and the critical state line at the same mean effective stress (Been and Jefferies 1985; Jefferies and

Been 2015) are amongst the most common methods of evaluating the potential for static liquefaction using conventional laboratory testing and in situ site investigation. However, a soil element in a slope can be subjected to complex boundary conditions compared to those imposed in laboratory tests, so that advanced and unconventional testing devices are required to partly simulate a realistic soil response in the laboratory. Furthermore, the abovementioned common methods of evaluating liquefaction potential do not consider some of the key factors in granular material behaviour, such as the effect of rate and magnitude of principal stress rotation, strain, and dilatancy rate on the instability and liquefaction. For example, Chu and Leong (2001) performed modified triaxial tests with controlled dilatancy rates to achieve instability in dilative sands, which was not a commonly accepted soil response based on conventional testing methods. Also, several studies that showed the soil response under rotational shear and constant deviatoric stress have highlighted the role of soil response associated with fabric and direction of major principal stresses (e.g. Oda 1972; Ishihara and Towhata 1983; Yang et al. 2007). Nevertheless, conventional (and unconventional) laboratory tests have limited loading and boundary conditions, whereas in situ tests suffer from uncertain loading and boundary conditions and, in most cases, excessive sample disturbance (Lade and Yamamuro 2011; Arshad et al. 2014).

In contrast to above methods, the applied physical modelling offers well-defined and diverse local boundary conditions (e.g. a combination of drained, partially drained, and undrained conditions), less constrained loading conditions (i.e. combined stress and strain-controlled loading), less soil disturbance, and a scale which is more representative of the inter-granular stress level. Moreover, it enables investigation of the hydro-mechanical processes in static liquefaction-induced flow slides, from initiation to large-scale flow slide, based on the observed soil response in the physical model experiments. The main goal of this research is to capture and describe the onset of instability in loosely packed submarine flow failures. For this purpose, the effects of the following factors on the initiation of flow slides and their consequent large-scale mechanical behaviours have been examined using physical modelling:

(i) Uniform change in the magnitude and direction of the in-plane principal stresses on the initiation of flow slides using a tilting mechanism;
(ii) Dependency of the failure on the rate of the principal stress change.

The paper is structured as follows: the "Experimental study" section describes the performed physical model tests, geotechnical properties of the sand, and experimental apparatus and instrumentations, followed in the "Test results" section by a detailed presentation of the experimental results. The "Discussion of the results" section discusses the test results, focusing on the effects of the controlling parameters on the global failure, as well as on the detailed monitoring of the onset of failure. Finally, the "Summary and conclusions" section summarises the research outcomes and conclusions.

Experimental study

Geotechnical properties of the sand

A fine clean silica sand known as Geba sand was selected for the experiments in this study. Table 1 presents a summary of its geotechnical characteristics. The drained internal friction angle was measured using direct shear tests and isotropically consolidated triaxial tests (Krapfenbauer 2016; Chavez Abril 2017; Steijlen 2019). In the direct shear tests, small weights were carefully maintained directly above the top cap of the shear box to apply the desired normal stress ranges. The permeability of the specimen was measured using the constant head method. Figure 1 illustrates the particle shape and grain size distribution of the sand.

The shape of the Geba sand grains was analysed using an image analysis technique. The roundness coefficient proposed by Wadell (1932), Eq. (1), was used for describing the particle shape:

$$R = \frac{\frac{1}{n}\sum_{i=1}^{n} r_i}{r_{max}} \tag{1}$$

where n is the number of particle corners, r_i is the radius of the i^{th} corner's curvature, and r_{max} is the radius of the largest inscribed circle in the particle (see Fig. 1a and b). Analysis of about 1000 Geba sand grains resulted in a roundness coefficient (R) of 0.77 ± 0.01 (where 0 and 1 represent fully angular and fully rounded particles, respectively). Therefore, the particles are categorised as sub-rounded.

Figure 2 presents the results of standard strain-controlled, isotropically consolidated, drained, and undrained triaxial tests on Geba sand. The soil specimens were prepared using the water pluviation technique. Prior to filling the triaxial test mould, the samples were kept fully submerged in a vacuum chamber to facilitate the saturation of the specimens. Due to the dilative undrained response of the sand during shearing together with the limited strain range of the triaxial setup, the critical state was not achieved in any of the tests. Such a dilative undrained response is commonly attributed to the soil grain shape and size distribution (e.g. Yang and Luo (2018)) plus the specimen preparation method (e.g. water pluviation technique). Generally a moist tamping specimen preparation technique is applied to obtain low relative densities in triaxial experiments. However, since such low relative densities are the result of large and non-uniformly distributed void sizes in the soil, a water pluviation method was selected here to produce more uniformly distributed pore sizes similar to the physical model test specimens that will be described in the following sections. The void ratio data corresponding to the phase transformation line (PTL) and the line connecting the data points at the end of each test (ETL) were taken as two rough approximations to the critical conditions. The phase transformation line (PTL) is the line drawn from the points at which the soil response changes from contractive to dilative (see Lade (1992)). As seen in Fig. 2a and b, the stress ratios of Geba sand for the PTL and the ETL were calculated, representing upper and lower bound approximations (1.14 and 1.33, respectively) for the critical state stress ratio and corresponding friction angle (which was estimated to be $\phi'_{critical} \approx 31°$). Meanwhile, based on the drained triaxial data, the correlations between the void ratio and mean effective stress for

Table 1 Material properties of Geba sand

Parameter	Value
Permeability (m/s) [at 30% relative density, constant head method]	4.2e-5
ϕ'_{peak} (degrees) [at 5–20 kPa confining stress range and Dr ~ 30%]	36
$\phi_{critical}$ (degrees) [estimated from undrained triaxial tests]	~ 31
Minimum void ratio, e_{min} [Japanese standard, JIS (2009)]	0.64
Maximum void ratio, e_{max} [Japanese standard, JIS (2009)]	1.07
D_{50} (μm) [wet sieve analysis, ASTM (2007)]	112
D_{10} (μm) [wet sieve analysis, ASTM (2007)]	85
D_{60} (μm) [wet sieve analysis, (ASTM 2007)]	125
C_u, uniformity coefficient [Lambe and Whitman (1991)]	1.12
C_c, coefficient of curvature [Lambe and Whitman (1991)]	1.14
Specific gravity, *Gs* [ultra-pycnometer 1000]	2.67
Fines content (silt) (%) [hydrometer test, ASTM (2007)]	4

the PTL (shown as a dashed line in Fig. 2c) and the ETL (shown as a solid line in Fig. 2c) were given by

$$e_{PTL} = 0.9907 - 0.0088 \ln p \quad (2)$$

$$e_{ETL} = 1.0946 - 0.0253 \ln p \quad (3)$$

TU Delft Geotechnical Tank (GeoTank)

The physical model tests reported in this paper were performed in a large-scale (2 m wide × 2 m high × 5 m long) inclinable GeoTank (GT) (for more details, see De Jager (2018)), which was developed based on the experience gained during tests with the Brutus tank at GeoDelft in the 1980s (Molenkamp and van Os 1987). This tank is the major experimental facility for a long-term research programme evaluating the quality of numerical simulation models for investigating the behaviour of dikes and embankments subjected to future sea level rise and climate change. The current first phase of the programme concerns the simple case of saturated submerged slopes. The side walls of the tank comprise two 40-mm-thick glass windows to reduce possible frictional boundary effects and to observe the soil deformations using side cameras. Figure 3a shows a schematic view of the GT. The setup is equipped with specific specimen preparation and loading mechanisms that will be explained in more detail in the following sections.

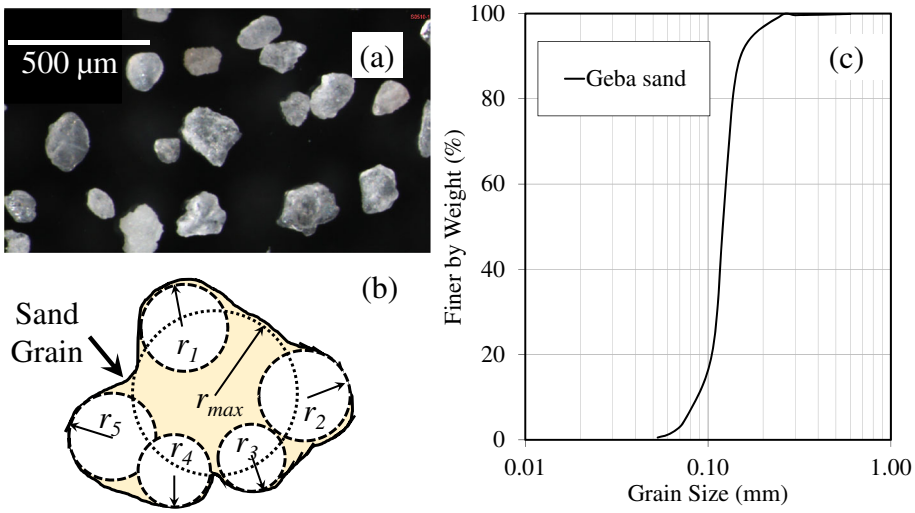

Fig. 1 **a** Sand particles; **b** particle shape analysis; **c** grain size distribution curve of Geba sand (after Krapfenbauer (2016))

Model preparation

The large dimensions of the GT and the mass of sand inside the tank (≈ 6500 kg) made the model preparation stage exceedingly challenging. Two primary goals of this stage were the reproducibility and maximum uniformity of the model properties. With this aim, a fluidisation technique was used.

The deposited sand in the GT (typically forming $h_o \approx 475$ or $h_o \approx 900$-mm-thick horizontal layers; see Fig. 3) was fluidised by the controlled upward flow of water (0.001 m^3/sec for $h_o \approx 475$ mm, and 0.0013 m^3/sec for $h_o \approx 900$ mm) through a network of perforated tubes installed on the base of the GT. A coarse granular soil layer and geotextile layers cover the fluidisation pipes to increase the uniformity of the pressure distribution. After the fluidisation, the sand layer was allowed to settle down under the self-weight of the particles. Figure 4a shows a schematic view of the fluidisation system.

During the fluidisation, the upward drag force of the pressurised water counterbalances the weight of the sand particles. Therefore, the sand bed thickness (h_o) starts to increase, depending on the intensity of the upward flow. The expansion of the sand layer (h/h_o) was monitored to ensure the consistency of the fluidisation stage before the experiments. Two target relative densities were selected for the experiments, these being a relatively loose ($Dr \approx 30 \pm 4\%$) state and a relatively dense ($Dr \approx 60 \pm 2\%$) state. Five 700-s consecutive fluidisation cycles at the discharge rate of 0.001 m^3/s were selected as the standard preparation stage for preparing the loosely packed specimens, which resulted in $h/h_o \approx 1.4 \pm 0.1$ (i.e. a maximum sand layer thickness of $h \approx 710 \pm 10$ mm for $h_o \approx 475$ mm). The dense specimens were produced by applying successive uniform water pressure shock waves to the entire sand body from the base of the GT after the end of the fluidisation process. The shock loads

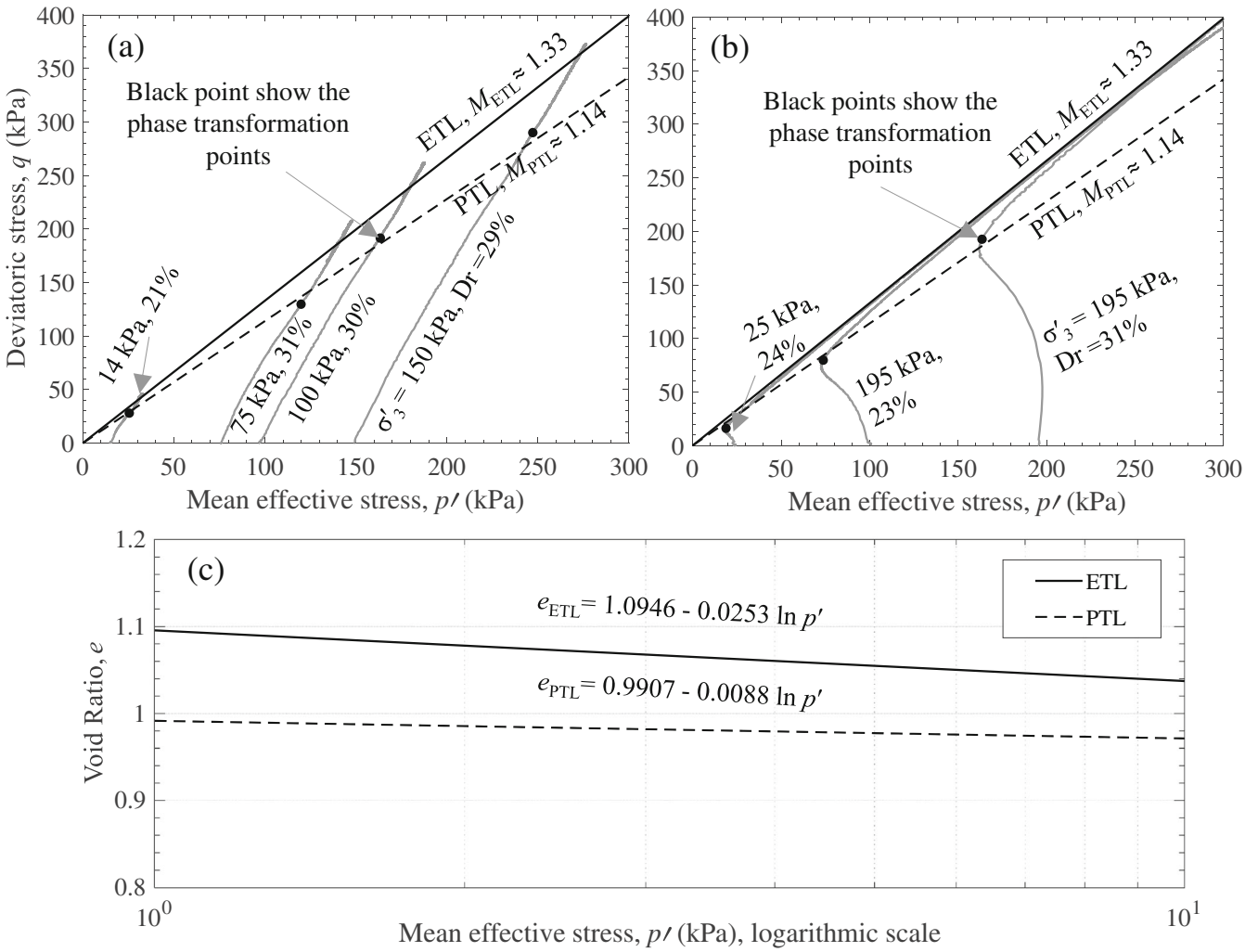

Fig. 2 Isotropically consolidated triaxial test results for Geba sand (after Steijlen (2019)): **a** stress paths in drained tests (with the effective confining pressure and relative density indicated for each test); **b** effective stress paths in undrained tests (with the effective confining pressure and relative density indicated for each test); **c** lower bound approximations of the critical void ratio as functions of the mean effective stress

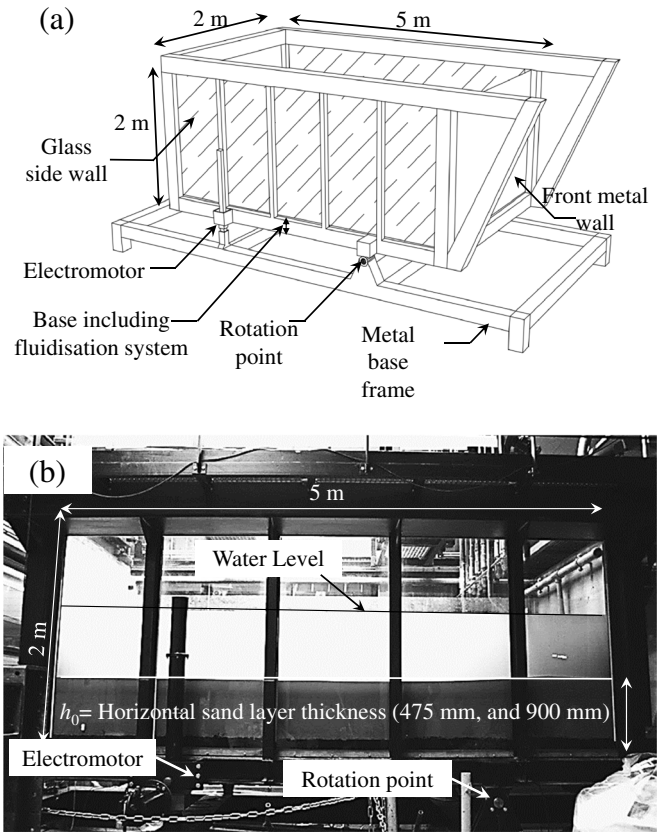

Fig. 3 Schematic view of the GT: **a** isometric view; **b** side view

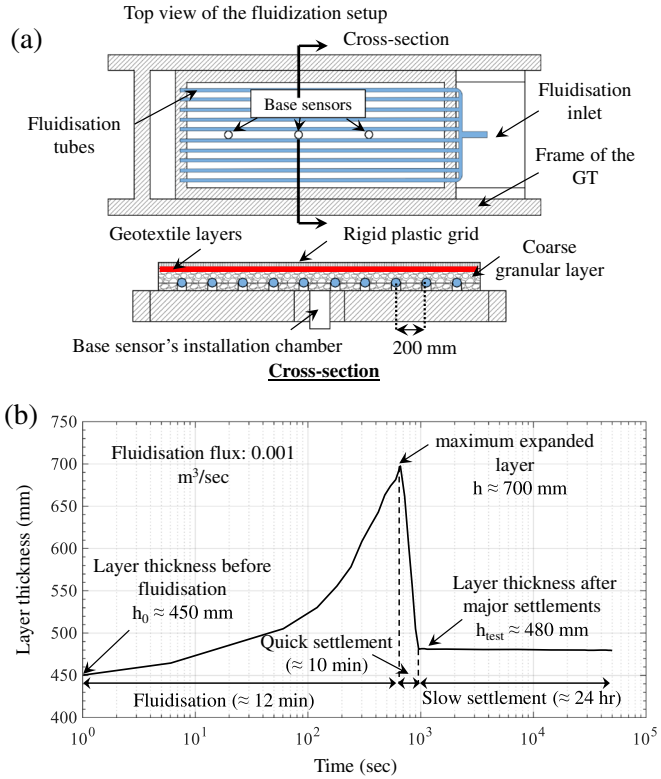

Fig. 4 **a** Schematic view of the fluidisation system at the base of the GT; **b** change in the layer thickness during and after fluidisation

were applied by short (5-s) upward pressure waves using the fluidisation pumps.

Figure 4b shows an example of settlement trends in the last cycle. Two consecutive settlement phases were observed after ending the fluidisation stage. The first phase was mainly the sedimentation stage, involving quick settlements of the extremely compressive sand suspension, which lasted about 10 min. The amount of settlement in the second phase was measured for 24 h and was found to have a negligible influence on the sand layer thickness (less than 1 mm in 24 h) and relative density. Therefore, a minimum 20-min waiting time was assigned prior to all of the tilting experiments, to eliminate the effect of rapid settlements in calculating the density after fluidisation and to ensure completion of the sedimentation phase. The 20-min waiting time is based on the moment the excess pore pressures have been dissipated and there are no noticeable settlements. This situation mimics a freshly deposited (very young) soil, such as a hydraulic fill, in which liquefaction flow slides often occur; see Robertson (2009).

Unlike other specimen preparation methods such as water and air pluviation, which are not feasible at the scale of the GT, the fluidisation technique suffers from segregation in the soil layer depending on the grain size distribution and the upward flow discharge rate. Segregation may cause inhomogeneity in some parameters, such as in permeability and the grain contact distributions in the soil profile. Table 2 summarises the change in the particle sizes at different depths after fluidisation in a horizontal sand layer ($h_o \approx 475$ mm) that implies a possible slight variation of permeability with depth. However, selecting a uniform material (e.g. Geba sand) and conducting the same model preparation procedure for all presented physical model experiments minimised the level of possible heterogeneities and resulted in practically the same conditions for all of the compared test results.

Instrumentation of the GT

Mobile sensors (MS)

A set of mobile sensors (MS) were developed with two separate embedded sensors that record the local pore pressure and accelerations in three perpendicular directions at a specific point in the sand layer. The accelerometer (Fig. 5a) can record an acceleration range of 2g ($-1g \leq Acc \leq 1g$) ± 0.005g, and the pressure sensor (Fig. 5b) can measure up to 50 kPa with a resolution of ± 0.075 kPa. Figure 5c shows a schematic view of the MS, in which the Z-direction is normal to the circular surface of the porous stone, the Y-direction is parallel to the data cable, and the X-direction is perpendicular to both Y and Z.

Figure 6b illustrates the installation steps of the mobile sensors in the reported experiments and Fig. 6c depicts a schematic view of the implemented installation pattern. A linear installation pattern along the centreline of the GeoTank was selected as the one which represents the overall kinematic of the ideally plane-strain inclined flat bed with minimum

Table 2 Grain size parameters at different depths after fluidisation of a 475-mm sand layer

Sample depth (mm)	D_{10} (mm)	D_{30} (mm)	D_{50} (mm)	D_{60} (mm)
0–50	0.079	0.109	0.116	0.12
50–100	0.086	0.11	0.119	0.124
100–200	0.084	0.109	0.118	0.123
200–300	0.092	0.113	0.122	0.127

boundary effects inside the GT. MS were suspended above the centreline of the GT using the data cables. The length of the data cables was arranged so that they could reach the desired depth within the sand layer (e.g. the middle of the sand layer). As shown in Fig. 6b and c, the sensors were installed above the tank before the fluidisation stage and they settled down along with the soil particles when the upward flow was terminated. This method ensured a minimum disturbance in the loose sand specimen due to installation of the sensors. It should be noted that, since the sensors were connected to flexible data cables, their location may not be exactly in the middle of the sand layer due to possible local bending of the cable.

Fixed sensors (FS)

Seven pore water pressure sensors were installed on the body of the tank (see Fig. 6a). These sensors were piezo-resistive pressure transmitters (KELLER PR-25Y) with vented gauges that read zero at atmospheric pressure. The pressure range recorded by the sensors was 50 kPa (± 0.02 kPa at 0–50 °C). The linearity of the sensors which represents the best fitted straight line to the recorded data, including hysteresis and repeatability in the records, was within ± 0.5% of the full measurement scale. Figure 6a shows the installation pattern on the setup. The sensors were labelled based on their location on the GeoTank (i.e. S South, N North, W West, E East, B base, and M middle). Throughout this paper, the upper and lower parts of the inclined GT will be referred to as the Southern and Northern ends, respectively.

Controlled loading mechanism

The loading mechanism and reproducibility of the applied loads in the experiments play an essential role in the observed soil behaviour at the onset of instability and the failure stage. The GT has three alternative loading mechanisms: a computer-controlled gradual inclination mechanism around a fixed rotation point, controlled pressure injection from the base of the tank, and plate loading of the crest for dredged slopes.

In this study, horizontal sand layers in the GT were sheared by the gradual tilting mechanism. The tilting mechanism was selected as it can be conducted at various rates and mimics an idealised

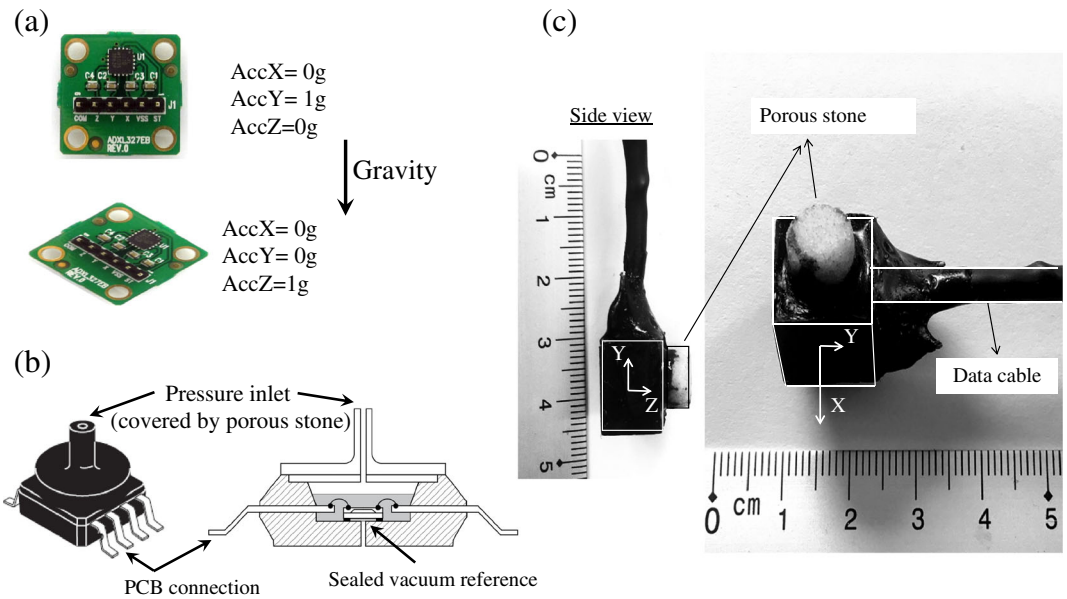

Fig. 5 Illustrations of **a** accelerometer chip (ADXL327) and two reference orientations with respect to gravity; **b** water pressure electronic sensor (MPX4250A) and its connection to the porous stone; **c** final assembly of the mobile sensor

condition where there is a uniform change in the direction and magnitude of the effective stresses in the field. This can be viewed as a simplified analogy of the steepening of scour hole slopes due to erosion (Zhang and Askarinejad 2019) or of the stress change in the slope due to a local surficial failure. A strong electro-motor was used for this purpose. The tank was titled as far as 10° to the horizontal at controlled fixed rates of R1 ≈ 0.01°/s, R2 ≈ 0.03°/s, and R3 ≈ 0.1°/s.

Test results

Table 3 summarises the physical model tests conducted in this experimental study, which investigated the impacts of the initial density of the soil and the shear loading rate on the static liquefaction potential of submerged sand layers at gentle angles. The tests were conducted on sand layers with two different relative densities of about 30% and 60% and two different layer thicknesses of about 475 mm and 900 mm. The horizontal sand layers were tilted at three different rates.

As illustrated in Fig. 7a, the flat sand bed showed two major responses in the tilting experiments; namely, stable and liquefied. The results indicated a high potential for static liquefaction-induced large plastic deformations at inclinations smaller than 10° in slopes of loose sand ($D_r \approx 30\%$), when the tilting rate was equal to or larger than 0.03°/sec for the 475-mm-thick layers and at all of the employed tilting rates for the 900-mm layers. Conversely, no failure (i.e. visible deformations or sudden change in pore pressure and acceleration data) was observed in the slopes of denser sand ($D_r \approx 60\%$), even at the highest tilting rate. It should be noted that this observation is limited to inclinations up to 10°, although the full structural range of motion is about 20° after removing the safety railings on top of the GT. Therefore, there is the possibility of observing failure in loose specimens at lower tilting rates at tilting angles higher than 10°. Figure 7b and c depicts the tilting of the tank in time using six reference states (P1 to P6), as well as the recorded pore pressure changes during tests 6 and 12. The presented data were recorded by the fixed base pressure sensors BN and BS (see Fig. 6a). In this example, the start of global failure in test 6 (Dr ≈ 31.4%) was identified by a major pore pressure jump at a slope inclination of 6.53°. The sand layer in the loosely packed soil tests was fully liquefied, and, post failure, it reformed as an extremely loose layer parallel to the water surface. The sand layer remained stable in test 12 and the pore pressure records showed only hydrostatic pore pressure changes due to tilting.

Figure 8 shows example data recorded by MS03 and MS08 in test 19 (see Fig. 6c). The pore pressure data showed a similar trend to all of the reported fixed sensors during tilting and at the time of failure. Rapid large deformations at the time of failure can be indicated by an abrupt change in the acceleration data, followed by fluctuating values that indicated the occurrence of large plastic deformations and directional acceleration of the soil mass around the sensors. This figure presents additional information on the post-failure acceleration and pressure response, such as post-failure pressure fluctuations due to wave formations, post-failure large deformations, and reconsolidation phases. However, this paper mainly focuses on the onset of failure and the initiation of the liquefaction-induced flow, rather than on wave formations and the reconsolidation phase.

Discussion of the results

Effect of the controlling parameters on the global failure

The physical model tests in this study consisted of two main phases. The first phase involved the experiments with fixed pore water pressure sensors (tests 1–15) to investigate the effect of the controlling parameters on the global failure of the soil. The second

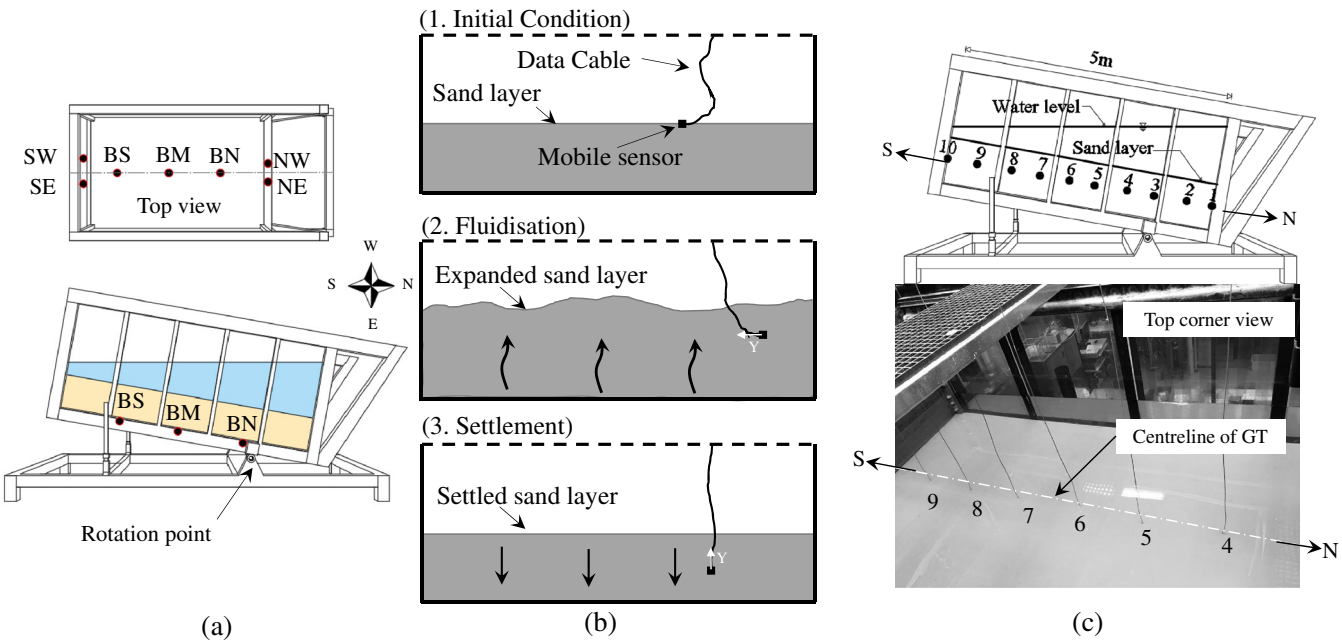

Fig. 6 **a** Fixed sensors' installation pattern; **b** schematic representation of the MS installation steps; **c** installation pattern of 10 MS along the centreline of the GT

phase involved the experiments with MS (tests 16–26), which mainly focused on the failure mechanism at the onset of failure. Figure 9 presents a more comprehensive illustration of the recorded pore water pressure changes in 6 representative experiments of the first set (tests 4, 5, 6, 10, 11, 12). The presented data include the pore water pressure response recorded by the fixed wall (NE, SE) and base (BN, BM, and BS) sensors in both the stable and liquefied sand layers.

The rate and density dependency of the failure points are the major observation in Fig. 9. The experiments with the stable response (e.g. tests 4, 10, 11, 12) showed a linear change in the water pressure due to the change in water level directly above each sensor, with the change in pore pressure depending on the location of the sensor with respect to the tank rotation point. The other experiments showed a sharp jump in pore pressure at the time of failure. After the peak generated excess pore pressure, fluctuating pressures due to sand-water mixture waves quickly became stabilised in the following reconsolidation phase. The wall sensors showed a similar response to the base pressure sensors at the time of failure, and it should be noted that the Southern wall sensors (e.g. SE) that did not show a large pressure peak were located underwater but out of the sand layer in the experiments with 475-mm sand layer depth. The recorded oscillations at failure in these sensors were due to the generated water waves and their reflections inside the GT.

Experimental evidence of the failure stages

The comparison of test results for various rates of tilting reveals the loading rate effect on the failure angle of the slope. Pore pressure changes recorded by fixed sensors, in two experiments with different rates of tilting but on specimens with similar relative densities, are presented in Fig. 10 and Figs. 15, 16, 17 in the Appendix. It is seen that pure hydrostatic water pressures were recorded from the beginning of the tilting up to points A and A' in

Table 3 Summary of the experiments

Test #	Tilting rate*	h_{ave} (mm)	*Dr* (%)	Void ratio (*e*)	Failure angle (°)	Soil response	Sensors**
1	R1	485	30.4	0.943	-	Stable	FS
2	R2	484	31.3	0.939	9.25	Liquefied	FS
3	R3	485	29.6	0.947	7	Liquefied	FS
4	R1	484	31	0.941	-	Stable	FS
5	R2	483	31.7	0.937	8.85	Liquefied	FS
6	R3	483	31.4	0.939	6.53	Liquefied	FS
7	R1	485	30.4	0.943	-	Stable	FS
8	R2	484	30.6	0.942	9	Liquefied	FS
9	R3	486	29.1	0.949	6.72	Liquefied	FS
10	R1	447	63.6	0.799	-	Stable	FS
11	R2	447	63.7	0.799	-	Stable	FS
12	R3	447	63.9	0.798	-	Stable	FS
13	R1	450	61.2	0.810	-	Stable	FS
14	R2	449	61.6	0.808	-	Stable	FS
15	R3	449	62	0.806	-	Stable	FS
16	R3	484	30.5	0.943	6.8	Liquefied	FS+MS
17	R3	488	27.4	0.956	6	Liquefied	FS+MS
18	R2	480	30.8	0.941	9	Liquefied	FS+MS
19	R3	924	27	0.958	6.4	Liquefied	FS+MS
20	R3	915	31	0.940	6.6	Liquefied	FS+MS
21	R1	909	34	0.928	9.9	Liquefied	FS+MS
22	R2	852	61.2	0.810	-	Stable	FS+MS
23	R1	859	58	0.824	-	Stable	FS+MS
24	R1	910	33.5	0.930	9.95	Liquefied	FS+MS
25	R3	910	33.5	0.930	7	Liquefied	FS+MS
26	R2	910	33.3	0.930	9.3	Liquefied	FS+MS

*R1 = 0.01°/s, R2 = 0.03°/s, R3 = 0.1°/s

**FS* fixed sensors, *MS* mobile sensors

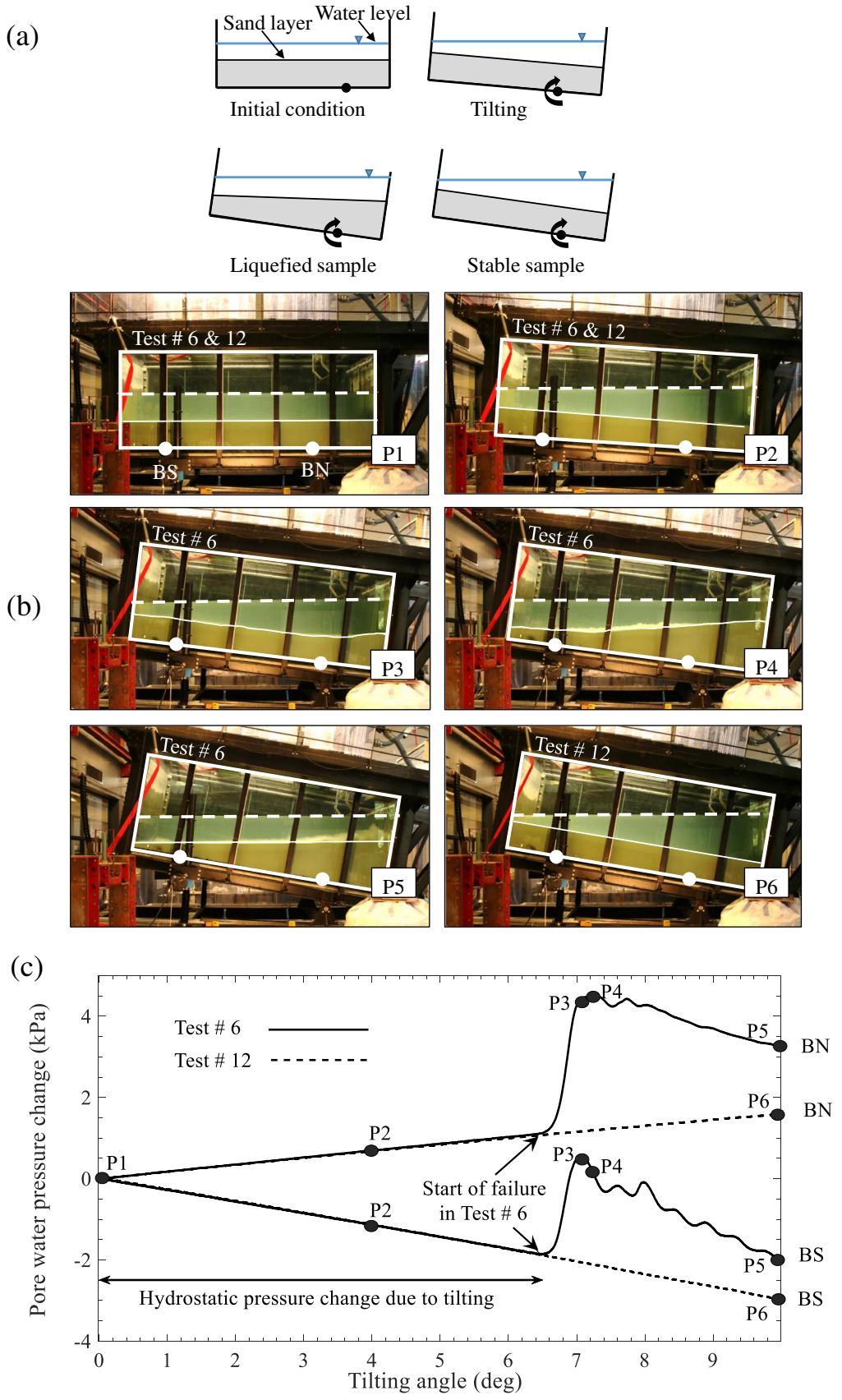

Fig. 7 **a** Two different global responses of the tilting experiments, stable and liquefied specimens; **b** photos during tilting of the tank in test 6 and test 12; **c** pore water pressure evolution recorded by sensors BN and BS in test 6 and test 12. (In the photos of the model tests in the GT, the solid lines represent the soil surface and the tank frame and the dashed lines indicate the water level)

both experiments. This portion of the data represented a fully drained condition with no excess pore pressure generation adjacent to the target sensor. By zooming in on the moment of failure (e.g. Fig. 10b and c), it can be seen that pressure jumps occurred in two consecutive phases. The first phase was a gradual but non-linear generation of excess pore pressure (i.e. paths AB and A'B' in b and c in Fig. 10, and Figs. 15, 16, 17 in the Appendix). This path represents a transition stage, from a fully drained state with practically negligible static deformations (purely hydrostatic, $P_{sensor}= P_{hydrostatic}$) to partially drained and undrained states reached after progressively increasing volumetric strains inducing the measurable excess pore pressure rise ($P_{sensor}= P_{hydrostatic} + P_{excess}$). As shown in b and c in Fig. 10 and Figs. 15, 16, 17 in the Appendix, subsequently, the gradual increase turned into a steep pressure jump up to a peak point (i.e. the paths BC and B'C'). The rate of the linear hydrostatic pressure change before the failure is associated with the location of the sensor and the rate of tilting in the experiments. Similarly, the higher rate of the pressure jump of path B'C' in comparison to path BC is mainly because of the kinematics of the slope failure at larger inclinations in the tests with a lower rate of tilting. This is understood to be due to the transformation of more significant potential energy to kinetic energy during path B'C' that generates the excess pore water pressure in the GT.

To further investigate the transition from the onset of instability to liquefaction-induced large deformations, the data recorded by the MS in the second phase of the physical model tests are now presented. As a representative example, Fig. 11 and Figs. 18, 19, 20 in the Appendix show the acceleration and pore pressure data recorded by four representative MS at the time of failure in tests 16, 18, 19, and 25, respectively. It can be seen that points B and B', as indicated on the pore water pressure data in the Fig. 10, coincide with the initiation of deformations recorded by the accelerometers. The pore pressure response recorded by the MS after the initiation of deformations is either a rapid increase (similar to the fixed sensors) or an apparent fluctuation, which is due to the movement of the sensor with respect to the liquefied sand around it, possibly affected by the connected data cables. Simultaneity of the start of deformations and the abrupt major changes in the recorded pore pressure trends are considered to be consistent with the abrupt occurrence of "instability", often indicated as "static liquefaction" and earlier depicted by points B and B' in Figs. 10, 15, 16, and 17. The subsequent post-instability paths BC and B'C' involve further intensification of structural collapses in the soil matrix along with the additionally generated excess pore pressure leading to liquefied flow.

Therefore, Figs. 11, 18, 19, and 20 show gradual local transitions (from A to B) during a time increment of about 1.0~1.9 (s) followed by large deformations. The sequence of the three observed events in the presented tests can be summarised as follows:

1) From point A to point B, the pore water pressure starts to increase gradually and progressively without the corresponding accelerations showing any sign of sudden change. This may indicate that the solid skeleton is experiencing a gradually and progressively increasing, small, rather homogeneous, irreversible contraction, possibly with grain-scale mechanical failures which are growing in size and generating increasingly larger excess pore water pressures. The pore pressure increase at this stage varies from about 0.3 to 3 (kPa) and shows various rates depending on the location and tilting angle of failure. Lower tilting (loading) rates showed shorter duration and higher rates of excess pore pressure generation due to higher failure angles that result in a quicker transition from stable to unstable conditions and a quicker and greater potential to kinetic energy transfer at the time of failure.

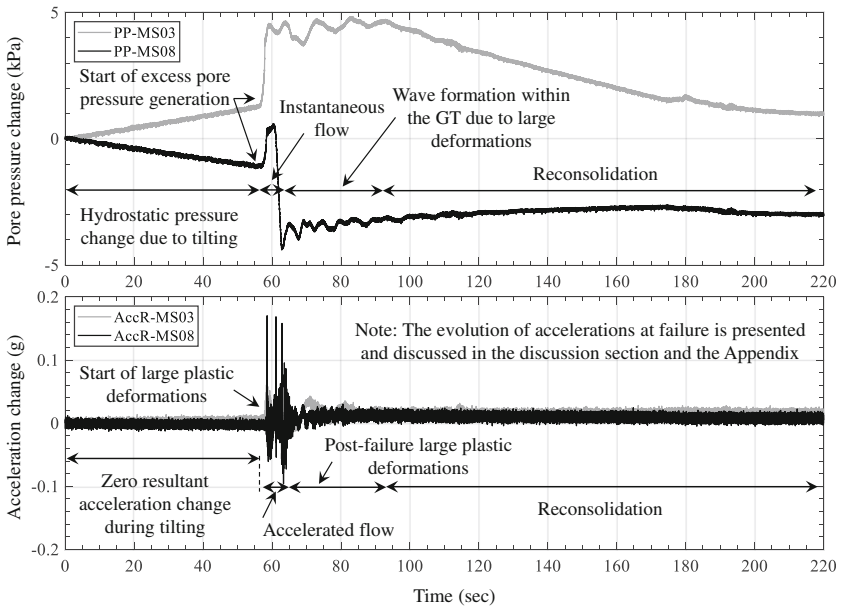

Fig. 8 Resultant acceleration and pore water pressure evolution recorded by sensors MS03 and MS08 in test 19

2) Then, the resultant accelerations suddenly start to show peaks during a period of about 0.2~0.6 (s) after point B. These peaks have magnitudes of about 0.01~0.08 (g) and durations up to about 0.05~0.1 (s). During the first part of this phase, the pore water pressure increases steeply at a rate of about 8 (kPa/s). It should be noted that the ranges in pressure and acceleration may be different to those highlighted for sensors at different locations and in tests with different rates of tilting.
3) Finally, as shown in Fig. 8, the pore water pressure reaches a somewhat steady upper limit of about 1.5 to 5 (kPa) and then starts to decrease, while the acceleration continues showing the same irregular peaks. This second part seems to involve the continuation of local irreversible deformation near the zero dilatancy state, with continuing deformation at almost constant volume. As a result, this phase seems to involve global post-stability liquefied flow, in which the accelerations intensify due to the growth in size of a locally liquefied zone (as seen previously in frame P5 of test 6 in Fig. 7b).>

Figure 12 shows a consistent time difference between the recorded jumps in pore pressure (starting time of the excess pore pressure, i.e. point A) and accelerations (starting time of the deformations, i.e. point B). The pore water pressures start the jump earlier than the accelerations in almost all the records. In this observation, a time interval between initiation of excess pore pressure and acceleration suggests that a transitional phase from a fully drained to a partially undrained condition intensifies the failure of particle assemblies and results in liquefaction of the loose sand layer. Additionally, it can be interpreted that the local instability seems to initiate at the beginning of the AB path, whereas the global instability, inducing the liquefaction and global dynamic flow, seems to occur after point B.

It is also essential to correlate the sequence of failure to the loading mechanism. The loading represented a mechanical (force-related) trigger that was mainly governed by a uniform change in the magnitude and direction of the principal stresses in the sand layer. It is now well established that the rotation of in-plane principal stresses significantly affects the soil strength behaviour under both monotonic and cyclic conditions, for both mechanical and hydraulic loading sources (e.g. Ishihara and Towhata 1983; Nakata et al. 1998; Lade et al. 2014; Yang et al. 2016).

Effective stress path in tilting-induced instability

The pore pressure data of the GT experiments revealed that, during rotational shear/tilting, the soil layer was being loaded under fully drained conditions up to the onset of instability (small irreversible contractions), whereupon an excess pore pressure rise was observed. After the onset of instability (e.g. point A in Fig. 10b), the local drainage conditions changed continuously, through

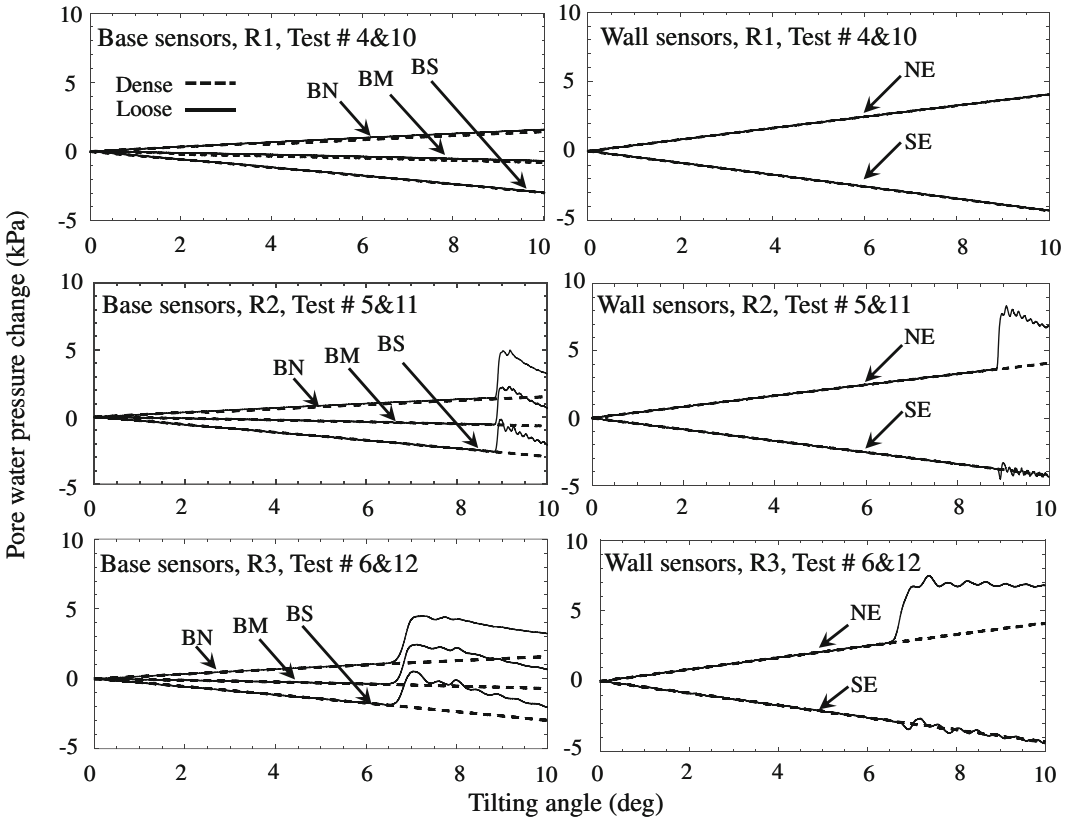

Fig. 9 Investigation of rate and density dependency of flow failure in the physical models with fixed pressure sensors

partially drained towards undrained, in a short time, and this led eventually to significant deformations and a liquefaction flow slide. Figure 13a qualitatively considers these phase transformations in effective stress paths of the GT experiments as visualised for an equivalent triaxial test, which may be similar to the stress paths of soil elements located in a slope in the field. The figure highlights the possibility of instability initiation in a fully drained condition. Note that the same type of behaviour has been observed in controlled, small-scale ("element") laboratory testing (e.g. Chu and Leong 2001). Chu et al. (2003) demonstrated that the zone of instability can be defined regardless of the drainage condition. Instability may occur under load-controlled drained or undrained conditions, as long as the stress path leads the stress point beyond the instability line. Figure 13b illustrates that the inclination of the instability line (and the extent of zone of potential instability) is not unique but highly dependent on the following factors as observed by responses in the GT experiments:

(i) Loading mode (e.g. rotational shear or triaxial shear), showing that soil instability may initiate at overly gentle slope angles (6–10°) in rotational shear/tilting, whereas, in engineering practice, instability friction angles are usually estimated under triaxial loading and are larger than 50% of the critical friction angle (~ 15°) (Jefferies and Been 2015). Rotational shear can be applied by monotonic tilting of a flat sand bed resulting in a gradual increase in the magnitude of, as well as a continuous rotation of, the principal stresses. In contrast, triaxial shearing leads to changing principal stresses relative to fixed principal stress directions.

(ii) Rate of the imposed loads, wherein faster rates of change in the magnitude and direction of the principal stresses results in a weaker soil response.

(iii) Relative density (see also Fig. 9), which has also been proven in small-scale experiments in previous studies (e.g. Yang 2002).

It should be noted that the observed rate-dependent instability is in contrast to the earlier findings of Yamamuro and Lade (1993). They indicated a minor effect of strain rate on the location of the instability line subjected to strain-controlled triaxial loading under both drained and undrained conditions. This discrepancy could be attributed to the use of strained-controlled loading in their triaxial experiments. The GT experiment results proved that a faster tilting rate results in an earlier transition from fully drained to undrained phases. Watanabe and Kusakabe (2013) reported a higher potential for transition to undrained behaviour at faster loading rates in their triaxial tests, which is in line with the observed response in the GT experiments.

Figure 14a shows the (global) void ratios of the soil in the GT experiments versus the angle of instability at which the first movement in terms of acceleration was detected by the sensors in the GT experiments. It can be seen that the angle of instability decreases with an increase in the void ratio. Figure 14a also shows the significant difference between the critical state friction angle roughly approximated by the angles of the ETL and PTL and the instability angle under rotational shear/tilting. Figure 14b presents the state parameter (Been and Jefferies 1985) calculated using the

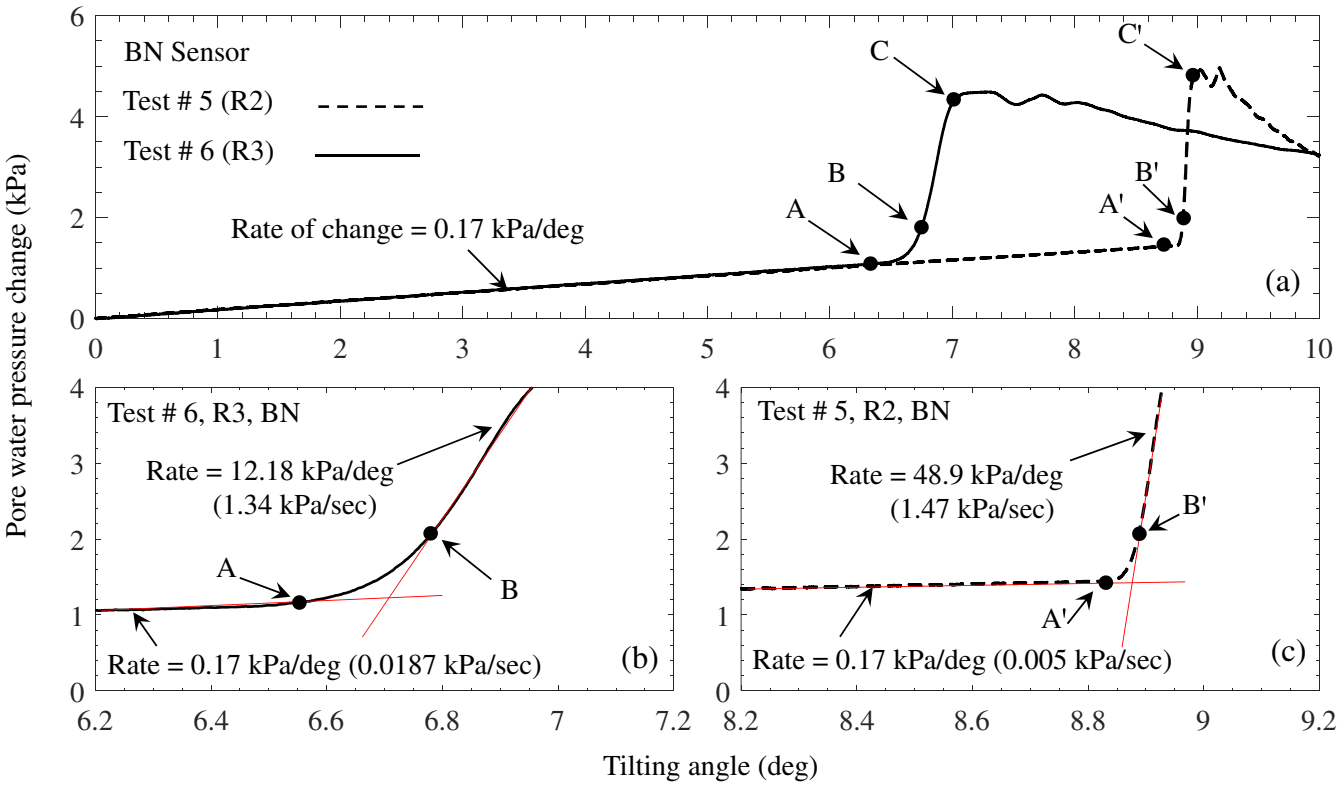

Fig. 10 Pore pressure recorded by the BN sensor for **a** the full range of motion in tests 5 and 6; **b** the point of failure in test 6; **c** the point of failure in test 5

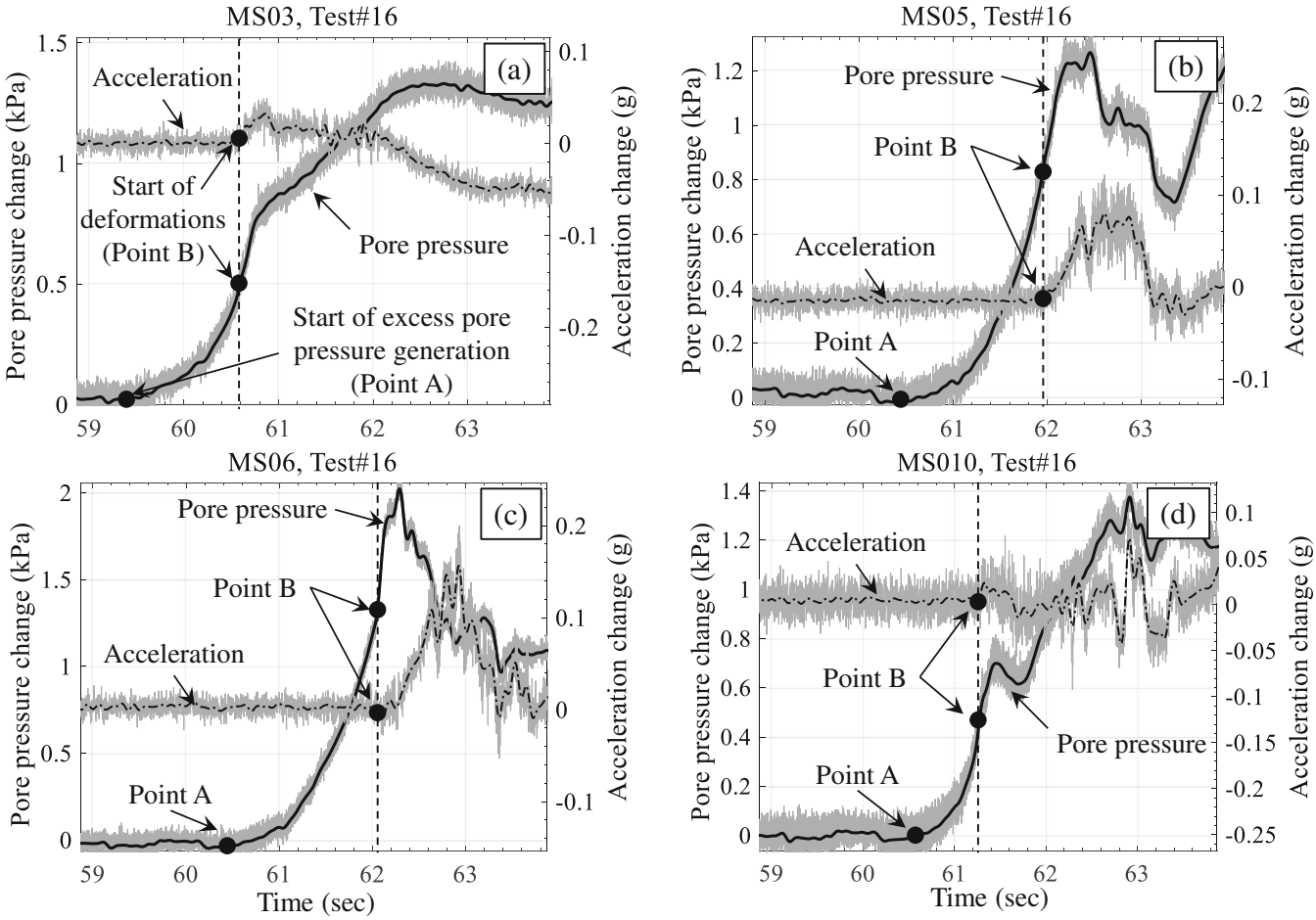

Fig. 11 Pore water pressure and resultant acceleration at the time of failure in test 16, recorded by **a** MS03, **b** MS05, **c** MS06, and **d** MS10

global void ratio in the GT experiments and the two lower bound approximations of the critical state condition as described in the "Geotechnical properties of the sand" section. However, it should be remembered that, because of the extremely low effective stress level in the GT, the critical state line in the *e*-log (*p*) plane may be significantly lower (see, e.g. Tatsuoka et al. (1986)) than those in Fig. 2 which are based on (much larger) engineering stress levels. The rough estimates in Fig. 14b indicate that the experimental data

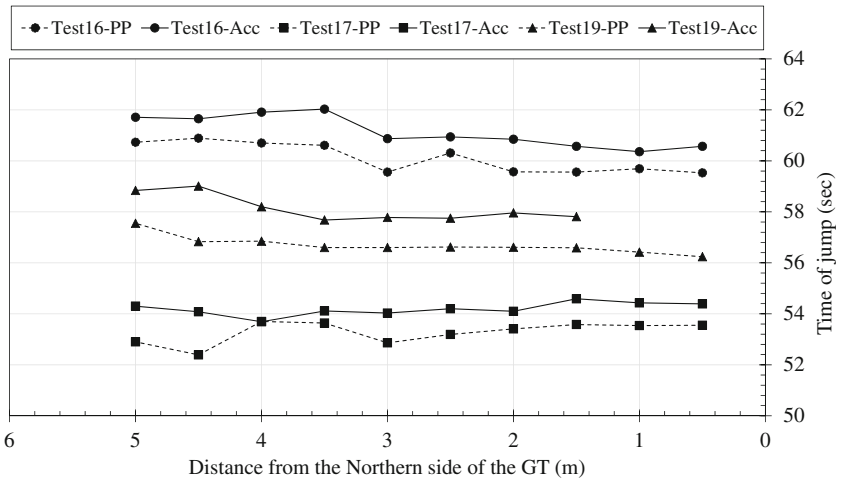

Fig. 12 Comparison of the times of jumps in acceleration and pore water pressure in three representative experiments (tests 16, 17, and 19)

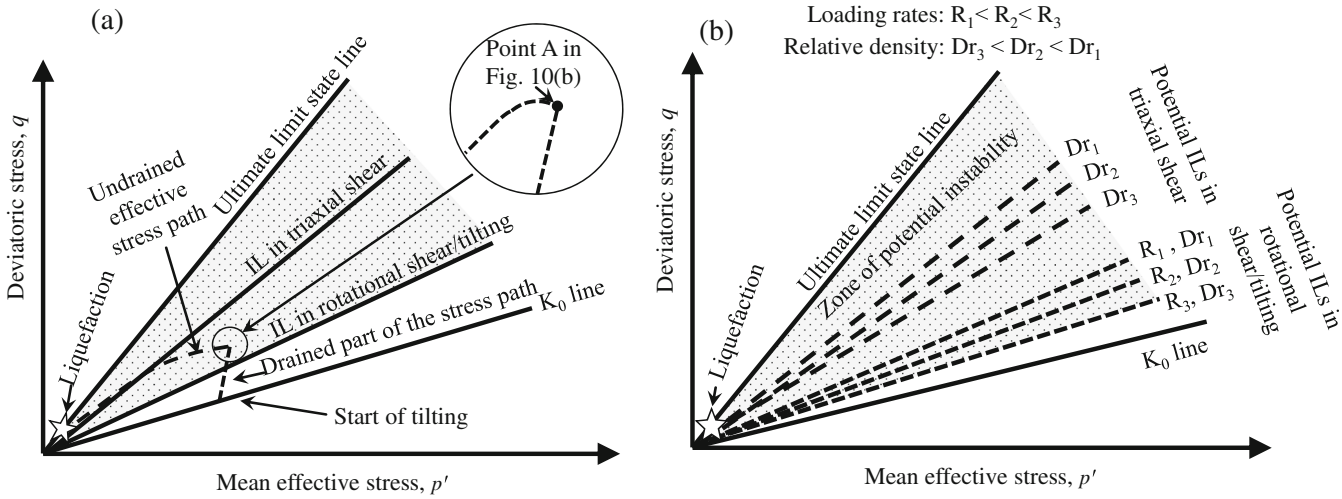

Fig. 13 Qualitative representation of **a** combined drained and undrained stress paths in the GT experiments, and of the position of the instability line (IL) in the GT experiments (rotational shear/tilting) and conventional triaxial shear; **b** rate and density dependency of the potential instability zone for two different loading conditions

points corresponding to the inclination of the GT at instability are located in the dilative range. This is because the practically common range of the state parameter corresponding to the transition from contractive to dilative behaviours is of the order − 0.05 according to Jefferies and Been (2015), and − 0.1 according to De Jager et al. (2008).

Of course, the behavioural characteristics of a sand can be measured in various laboratory apparatus, each inducing specific loading paths. These loading paths can be decomposed mathematically into two simultaneously changing components. One is the change in principal stresses relative to fixed principal stress directions and the other is the change in orientation of the principal stresses while keeping their magnitudes constant. At this point, it should be recalled that, at the critical state in a sand, i.e. at constant volume and stress during continuous distortion, the change in both the magnitude and orientation of these principal stresses needs to be zero in order for the stress to be constant. However, this does not exclude the possibility that, for a sand at the critical state, still an additional principal stress rotation can be applied, which will likely induce further densification of the sand

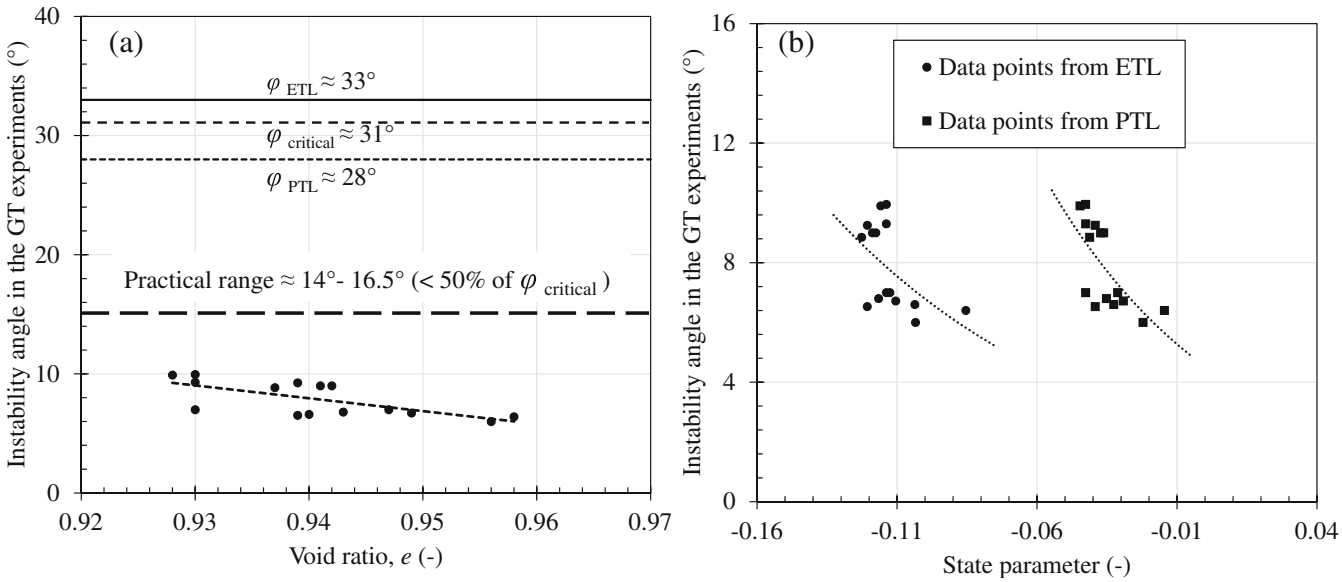

Fig. 14 State- and rate-dependant behaviour observed in the GT experiments based on the triaxial test data: **a** global void ratio of the GT tests versus instability angle in the GT experiments as reported in Table 3; **b** state parameter (derived from the estimated PTL and ETL rather than actual critical state line) versus instability angle in the GT experiments as reported in Table 3

skeleton (e.g. Yang et al. (2007)). Therefore, at this early phase of this investigation, the authors do not exclude the possibility that, even at more dilative states than critical, additional principal stress rotation may lead to additional compressive pore pressure generation.

It may therefore be concluded that, even though the presented sensor data show a clear picture of the soil response at the onset of instability for the specific loading mechanism and boundary conditions of the GT, a more advanced and non-conventional soil characterisation step is required for facilitating a more complete understanding of the test results and for providing relevant experimental data for constitutive models. To this aim, as a next step for utilising the current knowledge in practical applications and numerical validations, both modified triaxial and hollow cylinder devices with a fluidisation-like specimen preparation technique that better represents the GT experiments would be an ideal solution. The recommended advanced devices should also be equipped with low-range load and pressure sensors.

Summary and conclusions

The main objective of the presented research was to understand the instability mechanism of submarine slopes composed of loose sand and to examine the fundamental contributing factors to failure, such as the rate of change of the destabilising loads and the packing state of the soil.

Flow slides in loose sandy slopes occur due to static liquefaction, which is defined as the sudden loss of shear strength of the material due to fast, practically undrained, instability. Undrained instability can occur due to local collapses of the voids and the simultaneous generation of the excess pore pressure. These undrained collapses could happen due to additional static (shear) loads and/or change in the direction of principal stresses. In this study, static liquefaction was triggered by titling, which facilitates changes in both the magnitude and direction of the principal stresses. It was observed that minor perturbations in the direction and magnitude of the in-plane principal stresses in the loosely packed granular soil body can initiate global liquefaction in gentle submarine slopes. The unstable conditions are highly dependent on the rate of change in the direction and magnitude of these principal stresses.

At the onset of instability, the loose packing state of the soil may allow the spreading of local micro-failures and gradual minor contraction of the inter-granular structure and the corresponding excess pore pressure rise. Higher excess pore pressures will rapidly decrease the effective stresses and eventually lead to liquefaction of the soil. The liquefaction, and the excess pore pressure waves generated due to liquefaction, quickly transmit to the rest of the slope and result in a flow slide with large strains and significant runout distances. However, a denser packing in the soil may remain stable under the same stress changes and eventually lead to a progressive failure mechanism when loaded to much larger inclinations.

The following conclusions can also be drawn from this study:

- Static liquefaction-induced flow slides can be successfully physically modelled in a reproducible way at a large scale in the laboratory using the GeoTank. The experiments confirmed that a flow slide can be initiated in overly gentle slopes of less than 10° inclination.
- There was a consistent time delay between the start of excess pore pressure generation (point A, Fig. 10) and the start of fast and large plastic deformations (point B, Fig. 10), which highlights the transitional phase, from fully drained through partially drained towards the undrained phase at the occurrence of global instability, before the initiation of large deformations. Therefore, it can be suggested that the onset of instability is not limited to a local completely undrained boundary condition and that it can be initiated in a fully drained condition, depending on the loading mechanism and its associated grain interactions.
- Based on the very low instability angles in the physical model tests triggered by tilting of the GT, it can be concluded that conventional triaxial testing with fixed principal stress directions cannot properly reproduce the soil response of the tilted submerged sandy slopes (in the GeoTank). Therefore, more advanced soil characterisation with principal stress rotation is required for a better understanding of the instability in granular materials under more complex loading conditions. To this end, hollow cylinder torsional shear tests, enabling such principal stress rotation, will be better.
- The observed weaker soil response (i.e., complete soil liquefaction) in the GeoTank in comparison to conventional triaxial testing may be attributed to variability in the soil fabric, relative density and initial effective stresses, as well as to the aforementioned principal stress rotation.

Acknowledgement

The study is part of the project "Role of scour protection layers on static liquefaction induced flow slides", at Delft University of Technology, funded by Rijkswaterstaat (Ministry of Infrastructure and the Environment in the Netherlands). The current research was a follow-up study of a research project supported by the Dutch Technology Foundation STW, which is part of the Netherlands Organisation for Scientific Research (NWO). Also, the financial and technical support for the design and construction of the experimental facilities by Boskalis were much appreciated, in particular as given by Arjan Tanis and Ed van Ginneken. The experiments presented in this study would not have been possible without the help of Han de Visser, Kees van Beek, Ronald van Leeuwen, Marc Friebel, Jens van den Berg, Rein van de Oever, and Jan Graafland. The authors would like to thank Clemens Krapfenbauer, Miguel Angel Chavez Abril, and Florentine Steijlen (MSc students) for their help in the parameter determination and part of the experiments, and Dr. Faraz Sadeghi Tehrani for his constructive review and fruitful discussions.

Appendix

Figures 15, 16, and 17 present pore pressure changes recorded by fixed sensors, in two experiments with different rates of tilting but on specimens with similar relative densities. Figures 18, 19, and 20 show the acceleration and pore pressure data recorded by four representative MS at the time of failure in tests 18, 19, and 25, respectively.

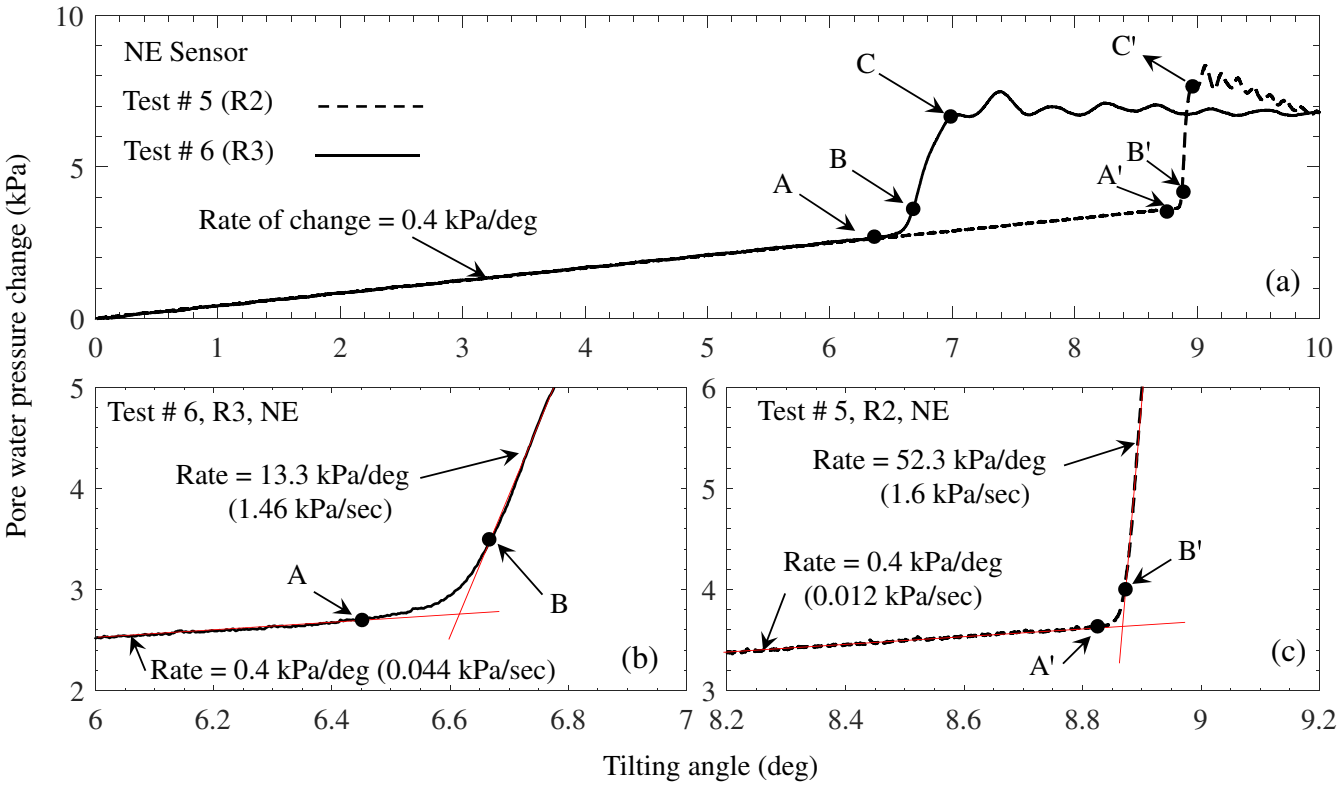

Fig. 15 Pore pressure recorded by the NE sensor for **a** the full range of motion in tests 5 and 6; **b** the point of failure in test 6; **c** the point of failure in test 5

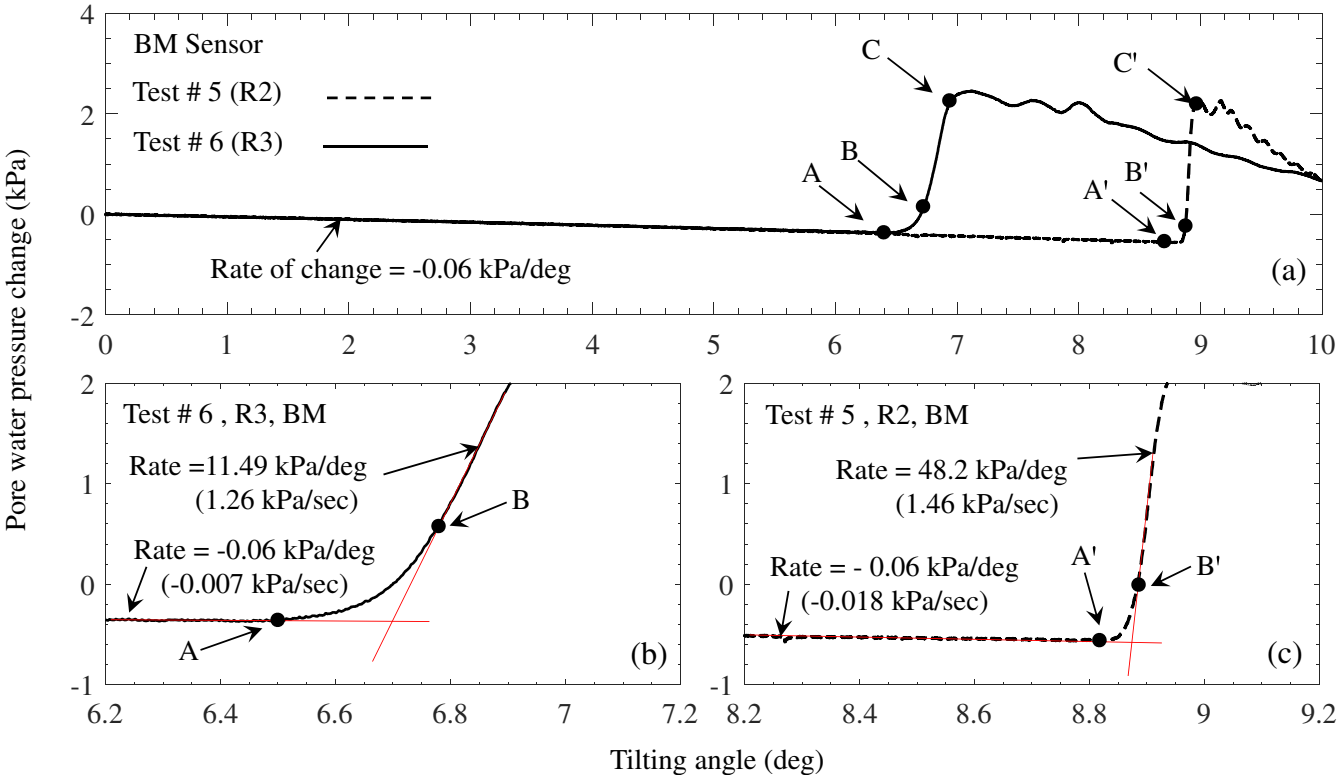

Fig. 16 Pore pressure recorded by the BM sensor for **a** the full range of motion in tests 5 and 6; **b** the point of failure in test 6; **c** the point of failure in test 5

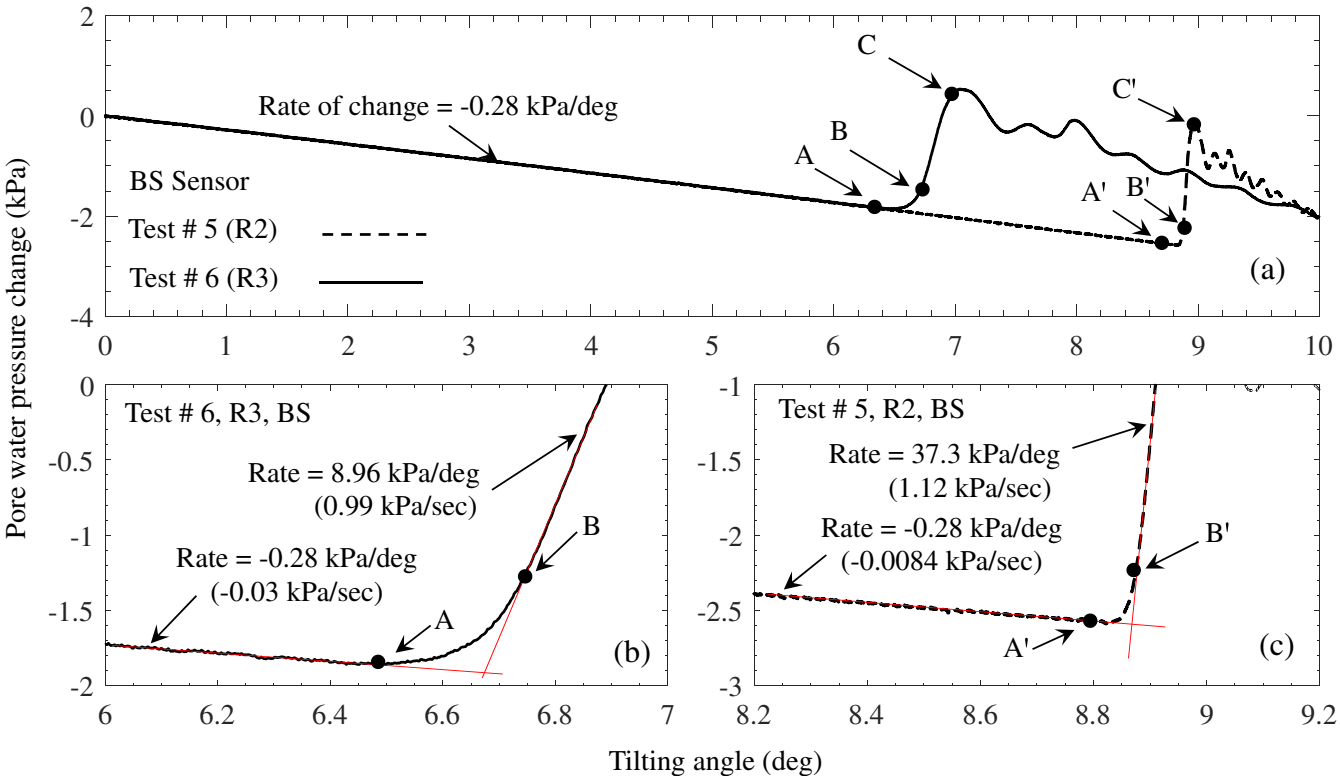

Fig. 17 Pore pressure recorded by the BS sensor for **a** the full range of motion in tests 5 and 6; **b** the point of failure in test 6; **c** the point of failure in test 5

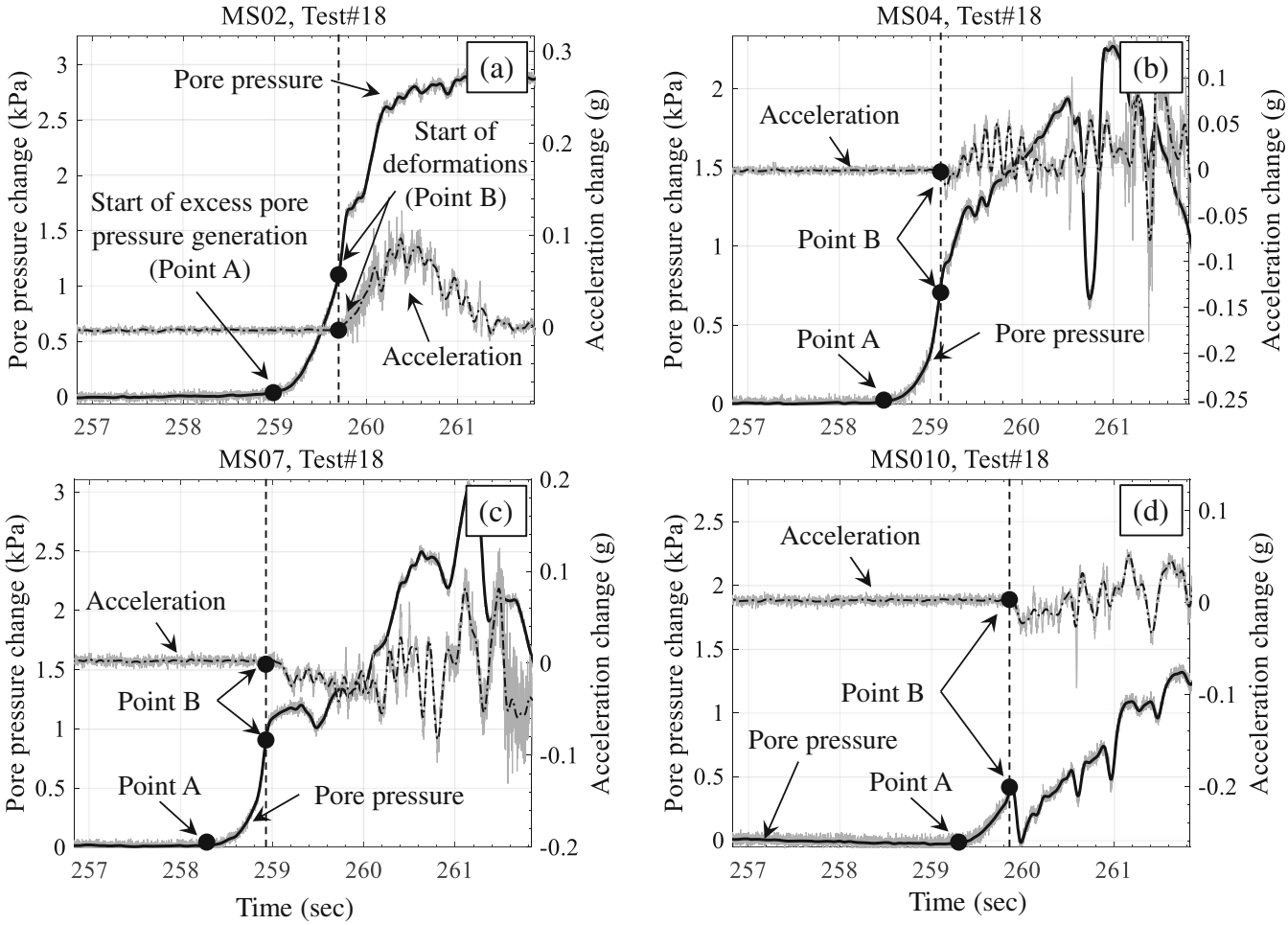

Fig. 18 Pore water pressure and resultant acceleration at the time of failure in test 18, recorded by **a** MS02, **b** MS04, **c** MS07, and **d** MS10

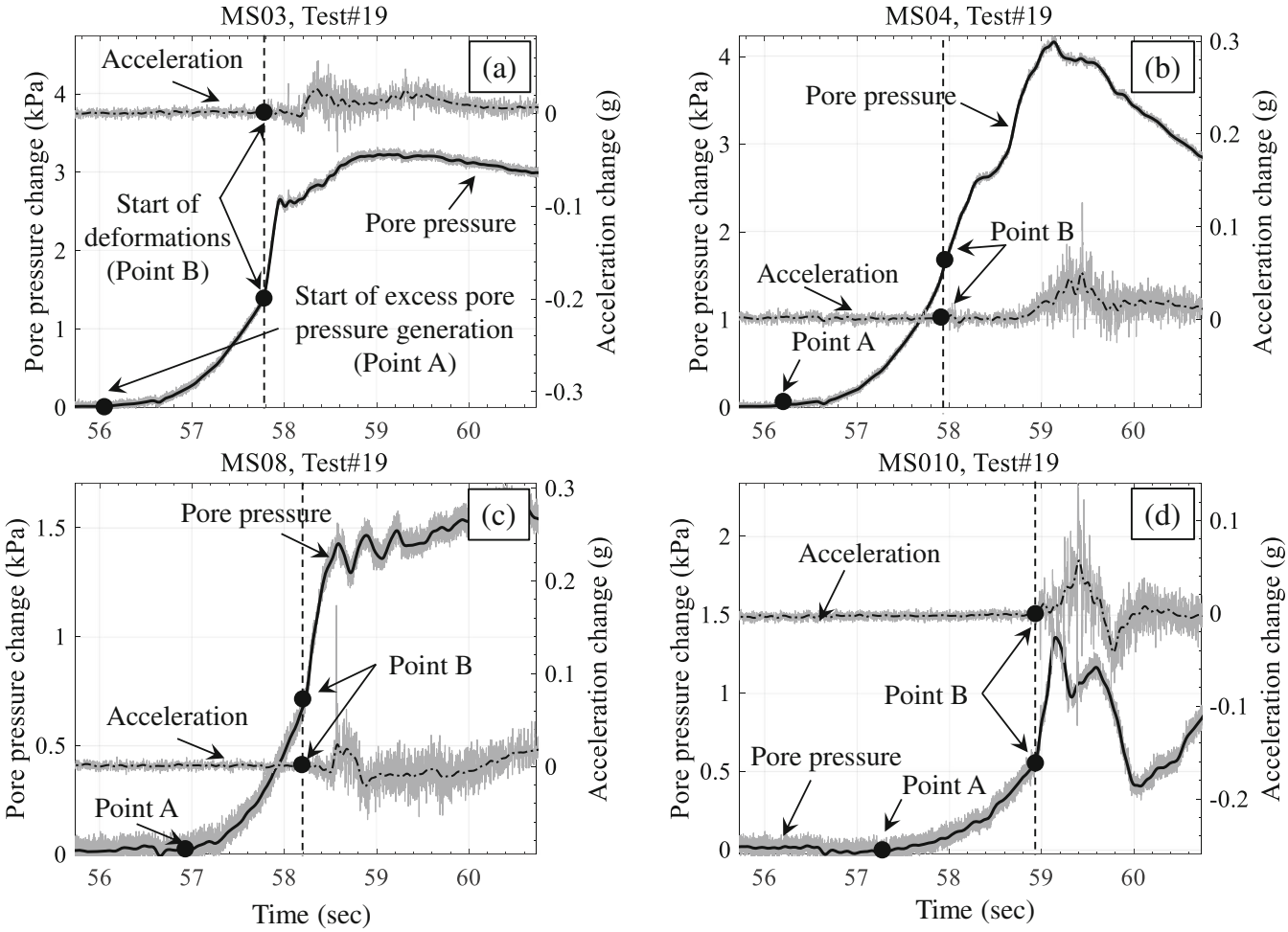

Fig. 19 Pore water pressure and resultant acceleration at the time of failure in test 19, recorded by **a** MS03, **b** MS04, **c** MS08, and **d** MS10

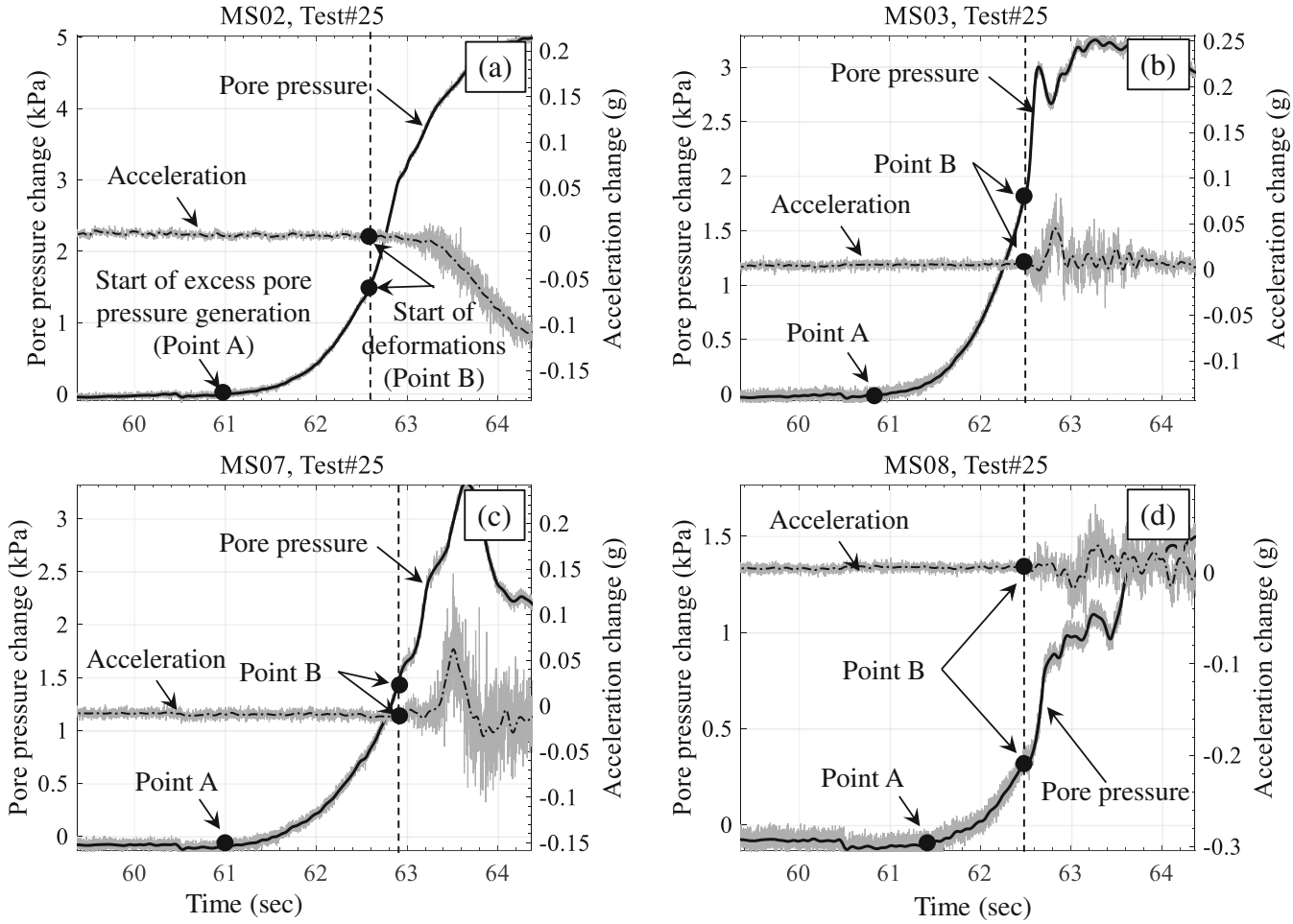

Fig. 20 Pore water pressure and resultant acceleration at the time of failure in test 25, recorded by **a** MS02, **b** MS03, **c** MS07, and **d** MS08

References

Arshad M, Tehrani F, Prezzi M, Salgado R (2014) Experimental study of cone penetration in silica sand using digital image correlation. Géotechnique 64:551–569. https://doi.org/10.1680/geot.13.P.179

ASTM International (2007) Standard test method for particle-size analysis of soils (Withdrawn 2016). http://www.astm.org/cgi-bin/resolver.cgi?D422. Accessed 2 May 2016

Been K, Jefferies MG (1985) A state parameter for sands. Géotechnique 35:99–112. https://doi.org/10.1680/geot.1985.35.2.99

Casagrande A (1936) Characteristics of cohesionless soils affecting the stability of slopes and earth fills. J Boston Soc Civil Eng 23:13–32

Chavez Abril MA (2017) Numerical simulations of static liquefaction in submerged slopes. M.Sc Thesis, Delft University of Technology

Chu J, Leong W (2001) Pre-failure strain softening and pre-failure instability of sand: a comparative study. Géotechnique 51:311–321. https://doi.org/10.1680/geot.2001.51.4.311

Chu J, Leroueil S, Leong W (2003) Unstable behaviour of sand and its implication for slope instability. Can Geotech J 40:873–885. https://doi.org/10.1139/t03-039

De Groot M, Lindenberg J, Mastbergen D, Van den Ham G (2012) Large scale sand liquefaction flow slide tests revisited. Paper presented at the Eurofuge 2012, Delft, Netherlands,

De Groot M, Lindenberg J, Mastbergen D, Van den Ham G (2019) Liquefaction flow slides in large flumes. Int J Phys Model Geo 19:37–53. https://doi.org/10.1680/jphmg.16.00026

De Jager R (2018) Assessing Liquefaction Flow Slides: Beyond Empiricism. Dissertation Delft University of Technology

De Jager R, Mathijssen F, Molenkamp F, van der Kolff AN (2008) Static liquefaction analysis using simplified modified state parameter approach for dredged sludge depot Hollandsch Diep. Paper presented at the 12th IACMAG

Dong Q, Xu C, Cai Y, Juang H, Wang J, Yang Z, Gu C (2015) Drained instability in loose granular material. Int J Geomech 16:04015043. https://doi.org/10.1061/(ASCE)GM.1943-5622.0000524

Hicks MA, Boughrarou R (1998) Finite element analysis of the Nerlerk underwater berm failures. Géotechnique 48:169–185. https://doi.org/10.1680/geot.1998.48.2.169

Hicks MA, Onisiphorou C (2005) Stochastic evaluation of static liquefaction in a predominantly dilative sand fill. Géotechnique 55:123–133. https://doi.org/10.1680/geot.2005.55.2.123

Ishihara K, Towhata I (1983) Sand response to cyclic rotation of principal stress directions as induced by wave loads. Soils Found 23:11–26. https://doi.org/10.3208/sandf1972.23.4_11
Jefferies M, Been K (2015) Soil liquefaction: a critical state approach. CRC press
JIS (2009) Test method for minimum and maximum densities of sands JIS A 1224
Koppejan A, Van Wamelen B, Weinberg L (1948) Coastal flow slides in the Dutch province of Zeeland. Paper presented at the the 2nd Conference on Soil Mechanics and Foundations Engineering, Rotterdam, Netherlands
Kramer S (1988) Triggering of liquefaction flow slides in coastal soil deposits. Eng Geol 26:17–31. https://doi.org/10.1016/0013-7952(88)90004-X
Krapfenbauer C (2016) Experimental investigation of static liquefaction in submarine slopes. M.Sc Thesis, Delft University of Technology
Lade PV (1992) Static instability and liquefaction of loose fine sandy slopes. J Geotech Eng 118:51–71. https://doi.org/10.1061/(ASCE)0733-9410(1992)118:1(51)
Lade PV, Nelson RB, Ito YM (1988) Instability of granular materials with nonassociated flow. J Eng Mech 114:2173–2191. https://doi.org/10.1061/(ASCE)0733-9399(1988)114:12(2173)
Lade PV, Rodriguez NM, Van Dyck EJ (2014) Effects of principal stress directions on 3D failure conditions in cross-anisotropic sand. J Geotech Geoenviron 140:04013001. https://doi.org/10.1061/(ASCE)GT.1943-5606.0001005
Lade PV, Yamamuro JA (2011) Evaluation of static liquefaction potential of silty sand slopes. Can Geotech J 48:247–264. https://doi.org/10.1139/T10-063
Lade PV, Yamamuro JA (2012) Analysis of submarine flow slides in fine silty sand. Paper presented at the GeoCongress 2012
Lambe TW, Whitman RV (1991) Soil mechanics vol 10. John Wiley & Sons
Lindenberg J, Koning H (1981) Critical density of sand. Geotechnique 31:231–245. https://doi.org/10.1680/geot.1981.31.2.231
Locat J (2001) Instabilities along ocean margins: a geomorphological and geotechnical perspective. Mar Pet Geol 18:503–512. https://doi.org/10.1016/S0264-8172(00)00076-3
Masson D, Harbitz C, Wynn R, Pedersen G, Løvholt F (2006) Submarine landslides: processes, triggers and hazard prediction. Phil Trans R Soc A 364:2009–2039. https://doi.org/10.1098/rsta.2006.1810
Mastbergen D et al (2016) Multiple flow slide experiment in the Westerschelde Estuary, The Netherlands. In: Submarine mass movements and their consequences. Springer, pp 241–249
Miyamoto J, Sassa S, Sekiguchi H (2004) Progressive solidification of a liquefied sand layer during continued wave loading. Geotechnique 54:617–629. https://doi.org/10.1680/geot.2004.54.10.617
Molenkamp F (1991) Discussion of "Instability of granular materials with nonassociated flow" by Poul V. Lade, Richard B. Nelson, and Y. Marvin Ito (December, 1988, Vol. 114, No. 12). J Eng Mech 117:930–933. https://doi.org/10.1061/(ASCE)0733-9399(1991)117:4(930.2)
Molenkamp F, van Os R (1987) Liquefaction test in the Brutus Tank. Tech. Rep. CO-218598, Delft Geotechnics, Delft, Netherlands. https://doi.org/10.4233/uuid:4f98a07b-164b-4287-a1e8-6643b962d5c1
Monkul MM, Lade PV, Etminan E, Senol A (2014) Compressibility as an indicator of liquefaction potential. Geotech Eng J SEAGS AGSSEA 45:73–77
Nakata Y, Hyodo M, Murata H, Yasufuku N (1998) Flow deformation of sands subjected to principal stress rotation. Soils Found 38:115–128. https://doi.org/10.3208/sandf.38.2_115
Oda M (1972) The mechanism of fabric changes during compressional deformation of sand. Soils Found 12:1–18. https://doi.org/10.3208/sandf1972.12.1
Olson SM, Stark TD, Walton WH, Castro G (2000) 1907 static liquefaction flow failure of the north dike of Wachusett dam. J Geotech Geoenviron Eng 126:1184–1193. https://doi.org/10.1061/(ASCE)1090-0241(2000)126:12(1184)
Puzrin AM, Gray TE, Hill AJ (2015) Significance of the actual nonlinear slope geometry for catastrophic failure in submarine landslides. Proc R Soc A 471:20140772. https://doi.org/10.1098/rspa.2014.0772
Robertson P (1999) Estimation of minimum undrained shear strength for flow liquefaction using the CPT. Paper presented at the International Conference on earthquake geotechnical engineering. Loisboa, Portugal
Robertson P (2009) Evaluation of flow liquefaction and liquefied strength using the cone penetration test. J Geotech Geoenviron Eng 136:842–853. https://doi.org/10.1061/(ASCE)GT.1943-5606.0000286
Sadrekarimi A (2014) Static liquefaction-triggering analysis considering soil dilatancy. Soils Found 54:955–966. https://doi.org/10.1016/j.sandf.2014.09.009
Sassa S, Sekiguchi H (2001) Analysis of wave-induced liquefaction of sand beds. Geotechnique 51:115–126. https://doi.org/10.1680/geot.2001.51.2.115
Silvis F, De Groot M (1995) Flow slides in the Netherlands: experience and engineering practice. Can Geotech J 32:1086–1092. https://doi.org/10.1139/t95-107
Sladen J, D'hollander R, Krahn J (1985) The liquefaction of sands, a collapse surface approach. Can Geotech J 22:564–578. https://doi.org/10.1139/t85-076
Steijlen F (2019) Experimental research of pore water pressure fluctuation on the stability of submarine slopes: a case study of the Eastern Scheldt storm surge barrier. M.Sc. Thesis, Delft University of Technology
Stoutjesdijk T, De Groot M, Lindenberg J (1995) Engineering approach to coastal flow slides. Coast Eng 1994:3350–3359
Stoutjesdijk T, De Groot M, Lindenberg J (1998) Flow slide prediction method: influence of slope geometry. Can Geotech J 35:43–54. https://doi.org/10.1139/t97-068
Sumer BM (2014) Liquefaction around marine structures. World Scientific
Tatsuoka F, Sakamoto M, Kawamura T, Fukushima S (1986) Strength and deformation characteristics of sand in plane strain compression at extremely low pressures. Soils Found 26:65–84. https://doi.org/10.3208/sandf1972.26.65
Terzaghi K, Peck RB, Mesri G (1996) Soil mechanics in engineering practice. John Wiley & Sons
Van Velzen G, Raaijmakers TC, Hoffmans GJC (2014) Scour development around the Eastern Scheldt storm surge barrier-field measurements and model predictions. Paper presented at the Scour and Erosion: Proceedings of the 7th International Conference on Scour and Erosion, Perth, Australia, 2-4 December 2014
Wadell H (1932) Volume, shape, and roundness of rock particles. J Geol 40:443–451
Watanabe K, Kusakabe O (2013) Reappraisal of loading rate effects on sand behavior in view of seismic design for pile foundation. Soils Found 53:215–231. https://doi.org/10.1016/j.sandf.2013.02.003
Yamamuro JA, Lade PV (1993) Effects of strain rate on instability of granular soils. Geotech Test J 16:304–313. https://doi.org/10.1520/GTJ10051J
Yang J (2002) Non-uniqueness of flow liquefaction line for loose sand. Géotechnique 52:757–760
Yang Z, Li X, Yang J (2007) Undrained anisotropy and rotational shear in granular soil. Géotechnique 57:371–384. https://doi.org/10.1680/geot.2007.57.4.371
Yang L-T, Li X, Yu H-S, Wanatowski D (2016) A laboratory study of anisotropic geomaterials incorporating recent micromechanical understanding. Acta Geotech 11:1111–1129. https://doi.org/10.1007/s11440-015-0423-7
Yang J, Luo X (2018) The critical state friction angle of granular materials: does it depend on grading? Acta Geotech 13:535–547. https://doi.org/10.1007/s11440-017-0581-x
Zhang W, Askarinejad A (2019) Centrifuge modelling of submarine landslides due to static liquefaction. Landslides 16:1921–1938. https://doi.org/10.1007/s10346-019-01200-z
Zhang W, Wang D, Randolph MF, Puzrin AM (2017) From progressive to catastrophic failure in submarine landslides with curvilinear slope geometries. Géotechnique 67:1104–1119. https://doi.org/10.1680/jgeot.16.P.249

A. Maghsoudloo (✉) · **A. Askarinejad** · **F. Molenkamp** · **M. A. Hicks**
Section of Geo-Engineering, Faculty of Civil Engineering and Geosciences,
Delft University of Technology,
Delft, Netherlands
Email: a.maghsoudloo@tudelft.nl

A. Askarinejad
e-mail: a.askarinejad@tudelft.nl

F. Molenkamp
e-mail: f.molenkamp@tudelft.nl

M. A. Hicks
e-mail: m.a.hicks@tudelft.nl

R. R. de Jager
Royal Boskalis,
Papendrecht, Netherlands
e-mail: Richard.de.jager@boskalis.com